RSC Advances

PAPER

View Article Online
View Journal | View Issue

Cite this: *RSC Adv.*, 2020, **10**, 11274

Enhanced visible light-mediated photocatalysis, antibacterial functions and fabrication of a 3-chlorophenol sensor based on ternary $Ag_2O \cdot SrO \cdot CaO$†

Md Abdus Subhan, *[a] Tanjila Parvin Rifat,[a] Pallab Chandra Saha, [a] M. M. Alam, [b] Abdullah M. Asiri, [c] Mohammed M. Rahman, *[c] Sonia Akter,[a] Topu Raihan,[d] A. K. Azad[d] and Jamal Uddin[e]

Received 7th February 2020
Accepted 3rd March 2020

DOI: 10.1039/d0ra01205j

rsc.li/rsc-advances

A novel multi-metal oxide nanocomposite, $Ag_2O \cdot SrO \cdot CaO$, was synthesized by a facile co-precipitation method followed by calcinations. The synthesized nanocomposite was characterized by XRD, FESEM, EDS, TEM, FTIR spectroscopy and photoluminescence (PL) spectroscopy. The composite showed enhanced photocatalytic activity under visible light irradiation and excellent anti-bacterial performance against both Gram-positive and Gram-negative bacteria. Here, the synthesized $Ag_2O \cdot SrO \cdot CaO$ nanomaterials were deposited on a glassy carbon electrode (GCE) in the form of a thin film to fabricate the desired electrochemical sensor and subjected to *I–V* analysis of 3-chlorophenol (3-CP) in a phosphate buffer solution (PBS). A calibration curve was plotted from the linear relation of current *versus* concentration and used to calculate the sensitivity (8.9684 μA μM^{-1} cm^{-2}), linear dynamic range (LDR, 0.1 nM to 0.01 mM) and lower limit of detection (DL, 97.12 ± 4.86 pM). The analytical parameters of the sensor such as response time, reproducibility and long-term stability in the detection of 3-CP were reliable. Finally, it was used to analyze real samples collected from various environmental sources and found to be acceptable.

1. Introduction

Mixed metal oxide nanoparticles are acquired by the combination of two or more metal oxides to give products with enhanced properties. Different metals having different oxidation states and electronic properties can combine in different proportions to give mixed metal oxide nanoparticles. The synthesized mixed metal oxide nanoparticles with modified physical, chemical, biological and morphological properties can have diverse applications.[1] Numerous synthetic processes have been developed for the synthesis of nano-metal oxides. The combination of two or more metals in a common metal oxide matrix can generate materials with novel structural and electronic properties.[2] SrO is an important wide band gap metal oxide semiconductor.[3] SrO is also used in the production of glass for color television tubes, ferrite magnets, small DC motors, pigments, dryers and paints.[4] Many methods such as chemical precipitation, hydrothermal and sol–gel approaches have been used for the synthesis of SrO.[5] Silver is a noble metal and due to its unique properties, it has a noticeable presence in the area of nanomaterial research.[6] It is well-known that silver ions and silver-based compounds have strong biocidal effects on many species of bacteria including *E. coli*[7] because they are highly toxic to microorganisms.[8] Ag_2O nanoparticles have been widely used in the field of oxidation catalysis,[9,10] fuel cells,[11] sensors,[12] photovoltaic cells,[13] all-optical switching devices, and optical data storage systems[14] and as diagnostic biological probes.[15] CaO is an alkaline earth metal oxide and has many applications as a catalyst,[16] toxic-waste remediation agent, doped material to modify electrical and optical properties,[17] refractory additive,[18,19] and crucial component in CO_2 capture[20–22] as well as in flue gas desulfurization and pollutant emission control.[23] The purification of hot gases is possible by alkaline-earth oxides, mostly calcium and barium-based oxides.[24] CaO nanoparticles are very applicable in industrial processes as a dehydrating

[a]*Department of Chemistry, School of Physical Sciences, Shah Jalal University of Science and Technology, Sylhet-3114, Bangladesh. E-mail: subhan-che@sust.edu; Tel: +8801716073270*

[b]*Department of Chemical Engineering and Polymer Science, Shah Jalal University of Science and Technology, Sylhet 3100, Bangladesh*

[c]*Center of Excellence for Advanced Materials Research (CEAMR), Department of Chemistry, Faculty of Science, King Abdulaziz University, P. O. Box 80203, Jeddah 21589, Saudi Arabia. E-mail: mmrahman@kau.edu.sa; Fax: +966-12-695-2292; Tel: +966-59-642-1830*

[d]*Department of Genetics and Biotechnology, Shah Jalal University of Science and Technology, Sylhet-3114, Bangladesh*

[e]*Center for Nanotechnology, Coppin State University, Baltimore, MD, USA*

† Electronic supplementary information (ESI) available. See DOI: 10.1039/d0ra01205j

agent in the creation of steel and in the biomedical field as a drug delivery system.[25] A recent study reported that a CaO–Ag-NPs@$CaCO_3$ nanocomposite showed strong antimicrobial activity against *Escherichia coli* and *Staphylococcus aureus*.[26] It is also used as an absorbent, water softener, and potential hydrogen regulator for wastewater and in fertilizers.[27] The properties of multi-metal composite oxides fabricated from the assembly of individual oxides make the materials potentially significant in the fields of electronic devices, catalysis, photocatalysis and nonlinear optical and semiconductor devices.[28–33] This paper describes the ternary metal oxide $Ag_2O{\cdot}SrO{\cdot}CaO$, which has enhanced photocatalytic as well as anti-bacterial activity compared to that of the three single oxides Ag_2O, SrO and CaO.

The tenacious contamination of surface water due to the growth of industrial activities at a high rate is a serious risk to the environmental ecological system. In this century, organic chlorinated compounds such as CPs are the most extensively used chemicals and they exhibit significant toxicity and carcinogenicity to humans as well as aquatic living organisms due to their non-degradation behavior.[34,35] For decades, 3-CP is an essential raw material for the formulation of pesticides, fungicides, herbicides, antiseptics and wood preservatives.[36,37] Therefore, the environment is continuously polluted by CPs from industrial waste effluents and agricultural activities. Subsequently, aquatic animals are affected by the toxicity of CPs, which eventually reaches humans through the food chain. Researchers have detected CPs in soil, water and human fluids recently.[38,39] As a result, CPs are listed as a priority toxic substance by the U.S. Environmental Protection Agency (EPA).[40–42] Methods with good reliability are necessary to detect CPs in the environment as well as in humans. Analytical methods that include the enzyme linked immunosorbent assay (ELISA),[43] gas chromatography/mass spectrometry,[44] high performance liquid chromatography,[45] spectrophotometry,[46] electrochemistry[47–52] and fluorescence spectroscopy[53] have been applied to detect such toxic environmental chemicals.

An electrochemical sensor in the *I–V* approach was fabricated by depositing the synthesized $Ag_2O{\cdot}SrO{\cdot}CaO$ nanomaterials on GCE with a binder, Nafion, and used for the detection of 3-CP in PBS. The calibration curve from the linear relation of the current *versus* concentration of 3-CP was established and the sensitivity of the sensor, LDR and DL were calculated. Moreover, 3-CP was applied successfully to identify the reproducibility, response time and long-term stability of the sensor. Finally, the sensor validation was performed by the analysis of real environmental samples. To the best of our knowledge, the synthesized $Ag_2O{\cdot}SrO{\cdot}CaO$ nanomaterials on GCE is the first material that has detected 3-CP in PBS. This paper illustrated the synthesis, characterization, photocatalytic activities, antibacterial activities and PL properties of a $Ag_2O{\cdot}SrO{\cdot}CaO$ nanocomposite.

2. Materials and equipment

Silver nitrate (Sigma Aldrich, Germany), strontium chloride (Fluka, Germany), calcium chloride (Sigma Aldrich, Germany), sodium carbonate (AR, BDH), and methyl violet 6B were purchased and used without any further purification. The analytical grade chemicals such as diethylmalonate (DEM), 3-methoxyaniline (3-MA), 3-methoxyphenol (3-MP), 2,4-diaminophenyl dihydrochloride (2,4-DAPDHCl), 3-methoxyphenylhydrazine hydrochloride (3-MPHydHCl), benzaldehyde, *m*-tolylhydrazine hydrochloride (*m*-THydHCl), 3-chlorophenol, 4-methoxyphenol (4-MP) and cinnamaldehyde were received from Sigma-Aldrich Company (USA). The mono- & disodium phosphate and 5% Nafion suspension in ethanol were also acquired from Sigma-Aldrich to complete this study. The spectroscopic measurements were carried out using a double beam UV-visible spectrophotometer (UV-1800 series, Shimadzu Corporation, Kyoto, Japan). A spectrofluorometer (Shimadzu Corporation, Kyoto, Japan) was used for the PL study of the nanocomposite. The pH of the experimental solution was measured by a pH meter (model pH's-25, Shanghai Rex Instrument Factory, China). The calcination of the metal oxide composite was performed with an electric muffle furnace. FTIR analysis was carried out using a spectrophotometer (Shimadzu, IRPrestige-21). The field emission scanning electron microscopy (FESEM) was obtained with a JSM-7100FT, which was equipped with a JED-2300 energy dispersive microanalysis system (EDS) for elemental analysis. Transmission electron microscopy (TEM) images was recorded with a JEOL JEM-1400 series at 120 kV. The electrochemical measurements were performed with a Keithley electrometer (6517A, USA).

3. Experimental

3.1. Synthesis of $Ag_2O{\cdot}SrO{\cdot}CaO$ nanocomposite

The $Ag_2O{\cdot}SrO{\cdot}CaO$ nanocomposite metal oxide was prepared by the standard co-precipitation of the corresponding carbonates from the aqueous solution of the metal salts. Initially, 0.25 M, 30 mL solution of each of $AgNO_3$ (1.274 g), $SrCl_2{\cdot}6H_2O$ (1.999 g), $CaCl_2$ (0.832 g), and a solution (1.00 M, 50 mL) of Na_2CO_3 (5.299 g) were prepared with distilled water. Then, $AgNO_3$, $SrCl_2{\cdot}6H_2O$, and $CaCl_2$ solutions were mixed in a beaker in a 1 : 1 : 1 ratio and the mixture was stirred vigorously at room temperature for five minutes. In the next part, the solution of 1.00 M Na_2CO_3 was added slowly to the above mixture with agitation until the precipitation of the carbonates of the metal salts was complete. The final mixture was stirred for 4 hours at 55–60 °C with constant stirring. Then, the white metal carbonate precipitate was filtered and washed several times with distilled water. After the filtration, the precipitate was dried at 220 °C for one hour in an oven. To obtain a multi-metal oxide nanocomposite, the obtained dried precipitate was calcined in a muffle furnace at 600 °C for five hours. As a result of the calcination, a metal oxide nanocomposite was formed from the carbonates.

3.2. Fabrication of GCE with $Ag_2O{\cdot}SrO{\cdot}CaO$ nanomaterials

A slurry of synthesized $Ag_2O{\cdot}SrO{\cdot}CaO$ nanomaterials in ethanol was deposited on a GCE as a thin film layer and allowed to remain under ambient conditions for drying. The binding strength of the $Ag_2O{\cdot}SrO{\cdot}CaO$ nanomaterial thin film was

enhanced by the addition of a drop of 5% Nafion suspension and then placed inside an oven for an hour at 35 °C. Within this period, the modified GCE was dried entirely. For assembling the sensor probe, the modified GCE and a simple Pt-wire were connected with the Keithley electrometer in the series manner, where the $Ag_2O{\cdot}SrO{\cdot}CaO$ nanomaterials/GCE and Pt-wire performed as the working and counter electrode, respectively. The electrochemical sensor based on this method consists of two electrodes only. The stock solution of 3-CP was diluted in deionized water to form a series of solutions with concentrations ranging from 0.1 mM to 0.1 nM. After that, the assembled sensor was applied to analyze the 3-CP in detail. A calibration curve was plotted as the current *versus* the concentration of 3-CP and using the slope of the calibration curve, the sensor sensitivity was measured. By the identification of the most linear segment on the calibration plot, the LDR was defined. The DL was calculated using a signal-to-noise ratio of 3. The Keithley electrometer was set at 1.0 second as the holding period and 10.0 mL of the buffer solution prepared from the equimolar concentration of mono- and di-sodium phosphate was kept constant in the *I–V* analyzing beaker through the experiments.

4. Results and discussion

4.1. Structural analysis of $Ag_2O{\cdot}SrO{\cdot}CaO$ nanocomposite

As illustrate in Fig. 1, the 2θ peaks observed at 25.67°, 27.705°, 33.246°, 36.55°, 41.8°, 42°, 45°, 51.849°, 54.724°, 57.8°, 62° and 76.5°are due to the presence of the monoclinic ($P2_1/c$) Ag_2O phase in this nanocomposite (PDF file number 77-1829).[54] Similarly, the presence of a SrO phase is observed by the 2θ peaks at 32°, 35.8°, 37.5°, 38.2°, 48°, 54.5°, 57.9°and 62°. The cubic ($Fm\bar{3}m$) crystalline nature and phase purity of SrO nanoparticles was determined by the presence of strong and sharp diffraction peaks that match well with the database (JCPDS file #6-520).[55] The presence of cubic ($Fm\bar{3}m$) CaO was also confirmed by 2θ peaks at 32.5°, 36.6°, 38.2°, 44.5°, 45.4°, 64.2°, 67.8°, 77.4° and 81.8° (JCPDS card no. 00-004-0777).[56] The obtained results revealed the phase purity and presence of Ag_2O, SrO, and CaO phases in the $Ag_2O{\cdot}SrO{\cdot}CaO$ nanoparticles. The particle size was found to be 89.5 nm using Scherrer's formula, $\tau = K\lambda/(\beta \cos\theta)$, where τ is the mean size, K is a dimensionless shape factor with a value of 0.94, λ is the X-ray wavelength (0.1506 nm), β is the line broadening at half the maximum intensity (FWHM) and θ is the Bragg angle.[21]

4.2. Surface and morphology study of $Ag_2O{\cdot}SrO{\cdot}CaO$

FESEM and EDS. FESEM images were collected at different magnifications to confirm both the morphology and distribution of $Ag_2O{\cdot}SrO{\cdot}CaO$ particles (Fig. 2a and b). Irregular morphologies and rough surfaces with a porous structure were observed, which may impart enhanced catalytic and antibacterial properties to the $Ag_2O{\cdot}SrO{\cdot}CaO$ heterostructure. As shown in Fig. 2b, the stabilizing components of the composite, SrO and CaO, are present on the surface of the Ag_2O sample. Further, the EDS data was obtained to examine the elemental composition in the composite. The atomic percentage of Ag, Sr, Ca and O in $Ag_2O{\cdot}SrO{\cdot}CaO$ was found to be 0.53, 8.16, 11.41 and 79.90, respectively, as shown in Fig. 2c (Table S1†).

TEM image of $Ag_2O{\cdot}SrO{\cdot}CaO$. Fig. 3 shows the TEM images of $Ag_2O{\cdot}SrO{\cdot}CaO$ heterostructure nanoparticles. The nanoparticles were observed by TEM while they are in an aggregated form. The average particle size of $Ag_2O{\cdot}SrO{\cdot}CaO$ is 6 nm. Because of the significant aggregation of SrO and CaO on Ag_2O, individual particles cannot be easily distinguished by TEM measurements.

4.3. FTIR study

The FTIR spectrum of the $Ag_2O{\cdot}SrO{\cdot}CaO$ nanocomposite is shown in Fig. S1.† The bands of the vibration modes of M–O and O–M–O (M = Ag, Sr, Ca) appeared in the lower energy region of 400–1000 cm^{-1}. The strong broad absorption peak at about 1445 cm^{-1} is assigned to the asymmetric stretching

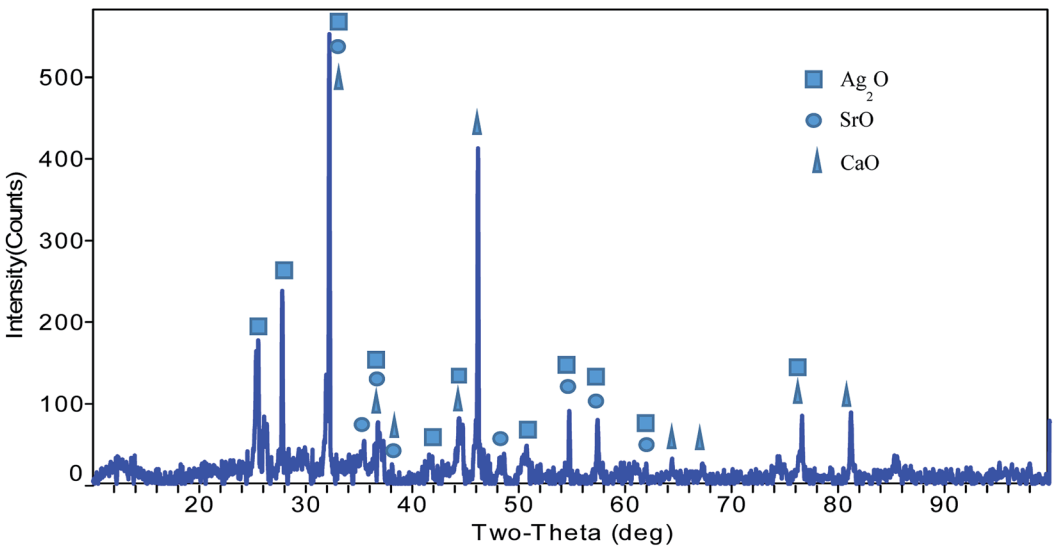

Fig. 1 X-ray powder diffraction pattern of $Ag_2O{\cdot}SrO{\cdot}CaO$ nanoparticles.

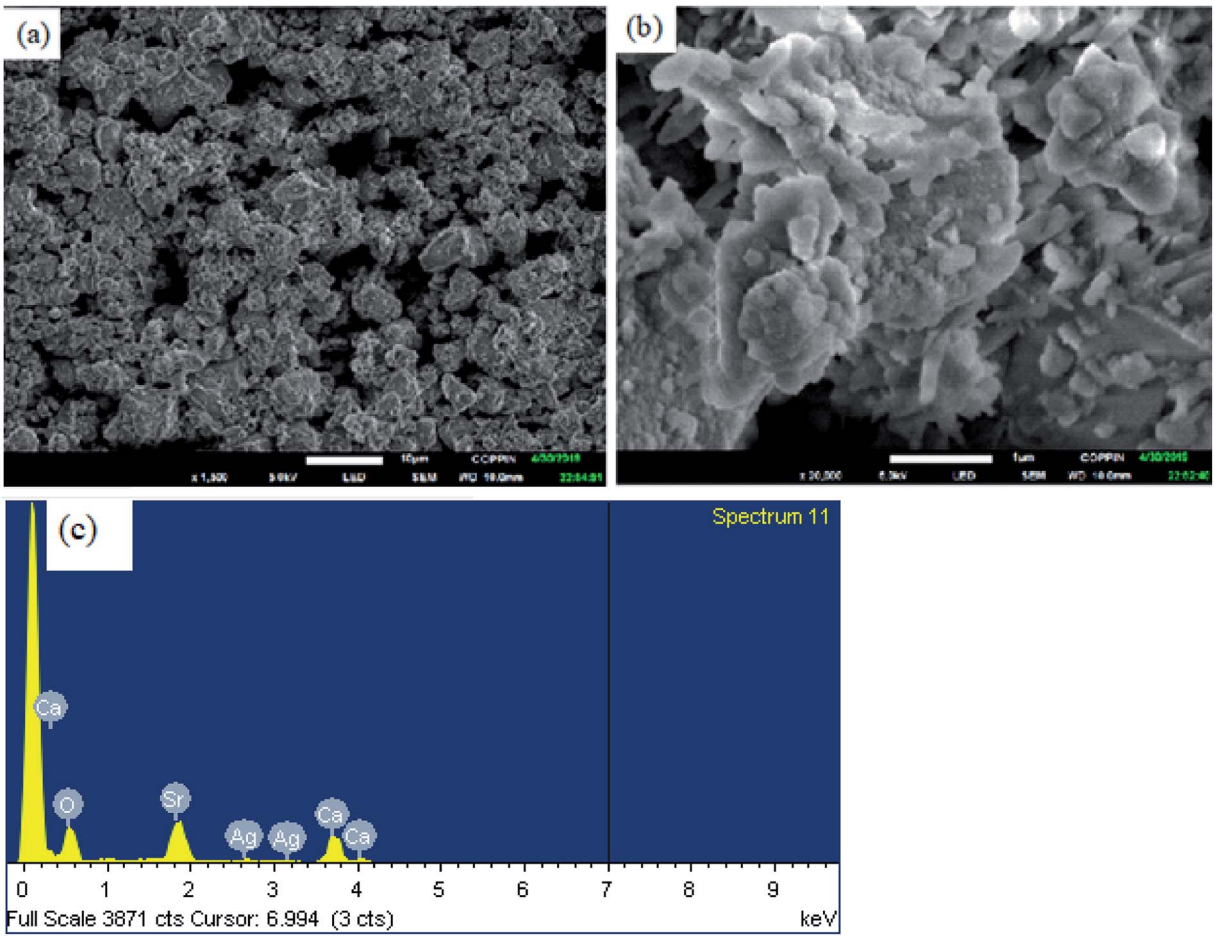

Fig. 2 Field emission scanning electron microscopy images (a and b) and energy dispersive spectrum (c) of $Ag_2O{\cdot}SrO{\cdot}CaO$.

vibration of Sr–O, and the sharp absorption bands at around 866 cm^{-1} are attributed to the out of plane bending vibration of Sr–O.[57] The IR band at around 666 cm^{-1} may be due to the low frequency Ag–O vibration. The peak observed at 706 cm^{-1} is assigned to the Ca–O vibration.

4.4. Photoluminescence study of $Ag_2O{\cdot}SrO{\cdot}CaO$ nanocomposite

The $Ag_2O{\cdot}SrO{\cdot}CaO$ nanocomposite was calcined at 600 °C and the PL spectra were collected in acetone at different excitation wavelengths (as shown in Fig. 4a). When the sample was excited at different wavelengths (294, 300, 330, and 350 nm), different emission peaks were observed, respectively. An intense emission peak along with other emission peaks was observed at 368 and 462 nm, respectively, when excited at 294 nm. Two emission peaks with low intensities were observed at 369 nm and 476 nm as a result of excitation at 300 nm. Then, when the sample was again excited at 330 nm, a relatively sharp emission peak was observed at 372 nm and another peak was observed at 410 nm. When the sample was excited at 350 nm, peaks were also observed at 384 and 430 nm as broad bands. In this study, when the sample was excited with increasing excitation wavelengths, the observed emission peaks in the UV-region showed a red shift. The data is compiled in Table S2.† These PL spectral emissions arise from the recombination of free carriers.

The $Ag_2O{\cdot}SrO{\cdot}CaO$ composite that was calcined at the same temperature also possessed excitation features when monitored at 380, 450, 480 and 500 nm, as shown in Fig. 4b. A strong sharp peak was observed at 333 nm when monitored at 380 nm. Two peaks were found at 331 and 352 nm with the monitoring wavelength of 450 nm. When the sample was monitored at 480 nm, a broad peak was observed at 350 nm and another one

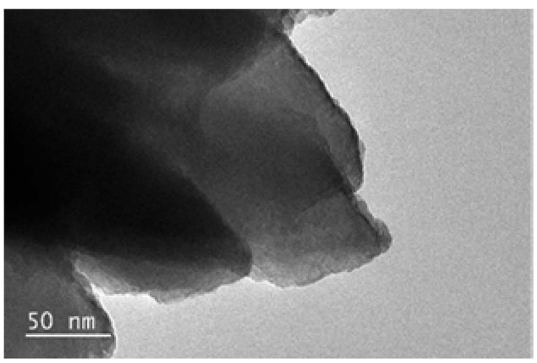

Fig. 3 Transmission electron microscopy image of $Ag_2O{\cdot}SrO{\cdot}CaO$.

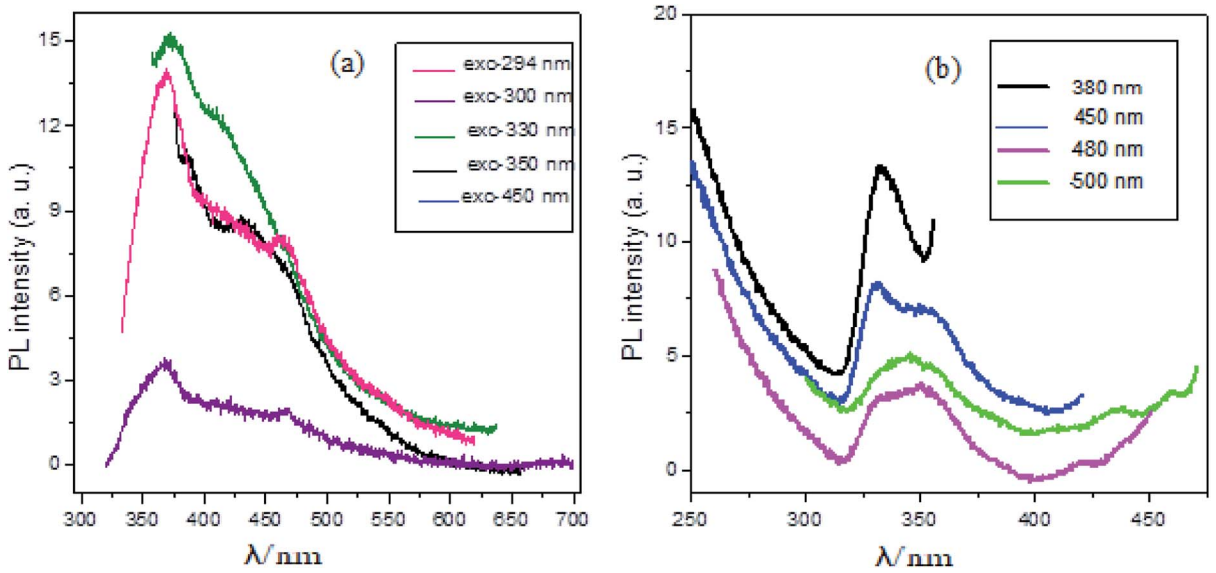

Fig. 4 PL spectra of $Ag_2O{\cdot}SrO{\cdot}CaO$ nanocomposite heated at 600 °C (a) at various wavelengths of excitations and (b) at various wavelengths of monitors.

was observed at 421 nm. A broad peak was also found at 345 nm with two other peaks at 435 and 459 nm when monitored at 500 nm. The data is compiled in Table S3.†

The PL of SrO, Ag_2O and CaO single metal oxide nanocomposites was also measured. All these nanocomposites were calcined at 600 °C. The PL spectra were measured in acetone at the same excitation wavelengths (Fig. S2†) as used for the $Ag_2O{\cdot}SrO{\cdot}CaO$ mixed metal oxide nanocomposites. The results revealed that the structure of the emission spectra, position and intensity of the emission peaks of $Ag_2O{\cdot}SrO{\cdot}CaO$ are different from that of the single oxides. The emission spectra of $Ag_2O{\cdot}SrO{\cdot}CaO$ are more well defined compared to that of the individual oxides. This is because mixing of SrO, Ag_2O and CaO in a composite oxide results in a perturbation of the energy levels that generates new luminescent centers in $Ag_2O{\cdot}SrO{\cdot}CaO$. However, observation of the much lower intensities of the emission peaks for $Ag_2O{\cdot}SrO{\cdot}CaO$ indicated that the recombination rate of photogenerated hole and electron pairs was lower in the heterostructure nanocomposite. Since PL emission arises from the recombination of free carriers, PL spectroscopy is the first choice to explore the mitigation, transfer and recombination processes of photogenerated electron–hole pairs in semiconductors. The PL results are presented in Fig. 4 and S2† wherein the corresponding single oxides clearly exhibited much stronger intensities than the nanocomposite, further indicating that the recombination of photo-induced electrons and holes in the $Ag_2O{\cdot}SrO{\cdot}CaO$ heterostructures can be effectively inhibited, which may improve the photocatalytic activity (see later).

4.5. Study of the photocatalytic activity of $Ag_2O{\cdot}SrO{\cdot}CaO$

Effect of distinct amounts of $Ag_2O{\cdot}SrO{\cdot}CaO$ photocatalyst on photodegradation. Initially, to make the stock solution of 1×10^{-4} M, 0.0393 g of methyl violet 6B (MV) dye was dissolved in 1000 mL of distilled water. To protect the dye solution from being degraded by sunlight, it was kept in the dark in order to shield the volumetric flask containing the solution.

Different amounts of $Ag_2O{\cdot}SrO{\cdot}CaO$ photocatalyst were taken to evaluate the effective dose for dye degradation under visible irradiation, as shown in Fig. 5 and S3.† Several amounts of the photocatalyst ranging from 0.03 g L^{-1} to 0.07 g L^{-1} were used to make different solutions in this study. The percentage of MV degradation gradually rose up to 0.05 g L^{-1} and then fell with increasing amounts of photocatalyst: 36%, 94%, 100%, 98% and 67% for 0.03 g L^{-1}, 0.04 g L^{-1}, 0.05 g L^{-1}, 0.06 g L^{-1}, and 0.07 g L^{-1} respectively. Thus, the efficiency began to decline after reaching the highest peak for the optimum dosage of 0.05 g L^{-1}.

4.6. Study of photocatalytic activity of $Ag_2O{\cdot}SrO{\cdot}CaO$ nanocomposite under visible light

An aqueous solution of MV dye was illuminated with a 200 W tungsten lamp in order to determine the photocatalytic activity

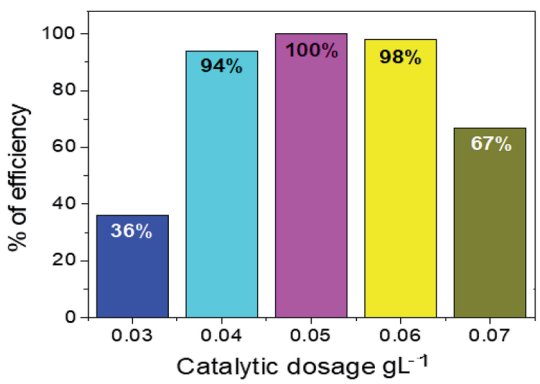

Fig. 5 Percentages of degradation efficiency of MV dye under visible light at distinct dosages of the nanocomposite; 0.03 g L^{-1}, 0.04 g L^{-1}, 0.05 g L^{-1}, 0.06 g L^{-1} and 0.07 g L^{-1} (MV concentration: 0.0393 g L^{-1}, pH 9, irradiation time 150 min).

of the $Ag_2O{\cdot}SrO{\cdot}CaO$ nanocomposite. A cylindrical Pyrex beaker of 5 cm in diameter was used to contain the MV solution and a fixed amount of the photocatalyst was added into that solution. The resultant solution was stirred in the dark for about 1 h before irradiation so that the adsorption–desorption equilibrium could be confirmed. After finishing the above step, about four mL of dye solution was removed into a tube at regular intervals and centrifuged prior to analysis in order to separate the dye solution from the photocatalyst. The spectrophotometric method was used to determine the change of dye solution concentration. The MV dye was degraded in the presence of the $Ag_2O{\cdot}SrO{\cdot}CaO$ photocatalyst at pH 9, 7 and 4, respectively. When the MV dye was degraded as a function of time, the spectroscopic measurements illustrate that the absorption intensity of MV dye declined over time in the presence of photocatalyst. According to Beer–Lambert's law, the concentration of MV is linearly proportional to the intensity of the absorption peak at 570 nm. Thus, by using the following equation, the photocatalytic efficiencies were calculated:[58]

$$\text{Photocatalytic efficiency} = (1 - C/C_0) \times 100 = (1 - A/A_0) \times 100.$$

Where, the concentration of MV dye before irradiation is denoted by C_0 and C indicates the concentration after irradiation time and the corresponding absorbances are denoted by A_0 and A, respectively.

The degradation of dye over time in the presence of the $Ag_2O{\cdot}SrO{\cdot}CaO$ photocatalyst at pH 9, 7 and 4 is shown in Fig. 6a–d and S4,† respectively. Fig. 6a shows changes in the absorption intensity of MV dye at pH 9 over time under visible light irradiation in the presence of $Ag_2O{\cdot}SrO{\cdot}CaO$. Similarly, Fig. S4a and b† show changes in the absorption of MV dye over time at pH 7 and 4, respectively. Fig. 6b reveals the degradation of dye over time and Fig. 6c represents the percent of efficiency at pH 9, 7 and 4, respectively. The degradation efficiencies were found to be 100%, 57% and 31% at pH 9, 7 and 4, respectively, after 120 min of visible light irradiation (Fig. 6d). Because of the formation of hydroxyl radicals at pH 9, it was found that the percent of dye degradation was excellent in basic media (pH 9), moderate in neutral media (pH 7) and inferior in acidic media (pH 4). MV is a cationic dye and is easily degraded in alkaline solutions rather than in neutral and acidic media.[58] The feasible reason for this promoted efficiency is that hydroxide ions are

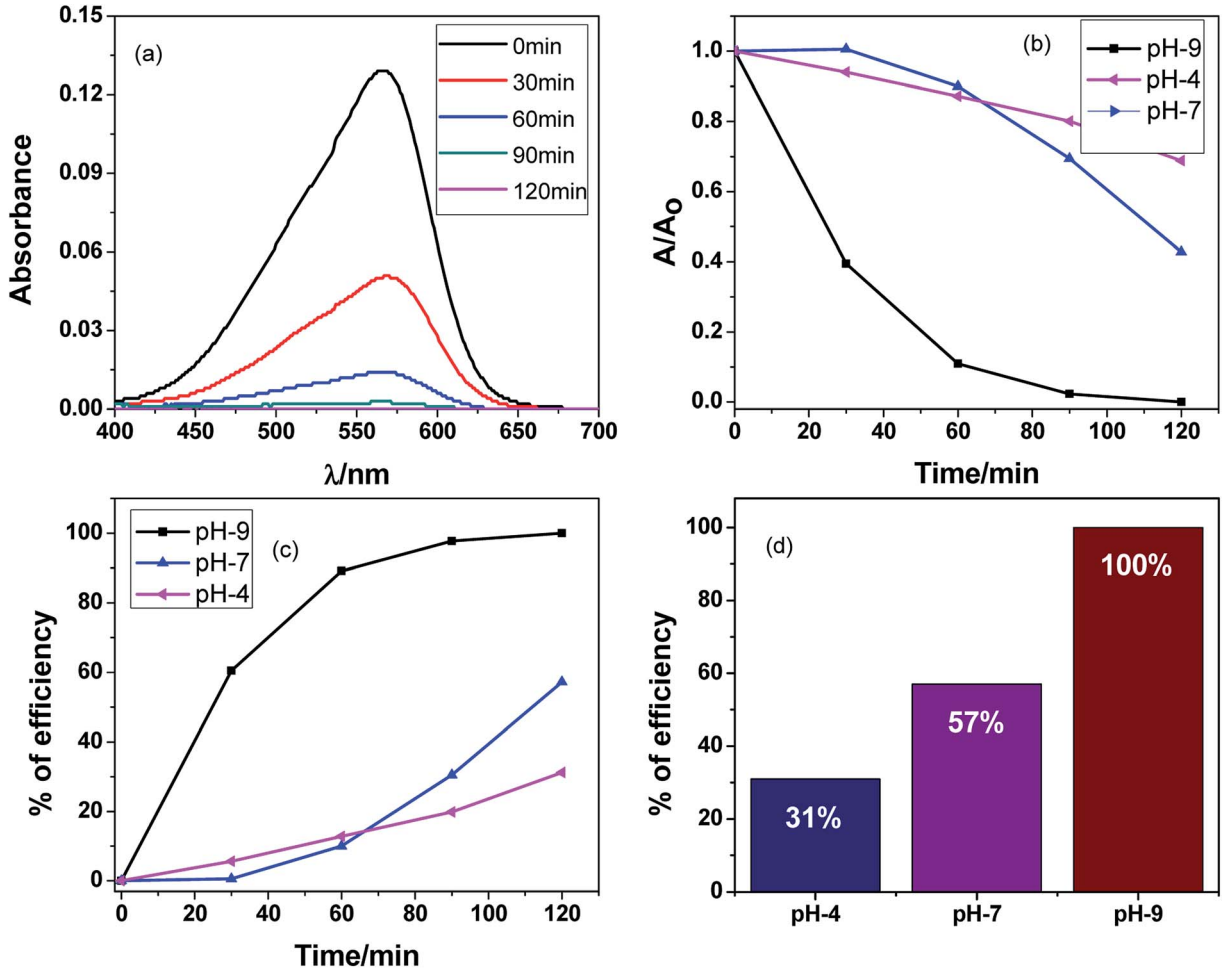

Fig. 6 (a) Variation in the absorption spectra of the photocatalytic degradation of methyl violet 6B dye in the presence of $Ag_2O{\cdot}SrO{\cdot}CaO$ under visible light irradiation for 120 minutes with 30 minute time intervals at pH 9, (b) degradation of dye over time and (c) percent efficiency with time (d) percent efficiency of dye degradation at different pH (MV concentration: 0.0393 g L^{-1}, catalyst dosages: 0.05 g L^{-1}).

easily oxidized into hydroxyl radicals in alkaline solution. It has been proposed that a Schottky barrier is formed at the interface between the metal and semiconductor, while defects are created within the crystal by the inclusion of one oxide to other oxides.[59] The catalyst produced active oxygen species in addition to scavenging the photogenerated electrons during the photocatalytic oxidation reaction in the presence of oxygen. So, hydroxyl radicals are formed and the defective metal oxides could respond to visible light by visible light-induced photocatalysis, which is widely employed for environmental remediation.[60–64]

4.7. Comparison of efficiencies of photocatalytic activity between $Ag_2O{\cdot}SrO{\cdot}CaO$ and its corresponding single metal oxide nanocomposites (SrO, Ag_2O, and CaO)

A similar procedure was followed to measure the photocatalytic activity of SrO, Ag_2O and CaO as with the $Ag_2O{\cdot}SrO{\cdot}CaO$ nanocomposite. The MV dye was degraded several times in the presence of SrO, Ag_2O and CaO single metal oxide photocatalysts at pH 9 under visible light irradiation and the observed results are shown in Fig. 7a–d and S5.† In each case, the change in the concentrations of dye solution was measured by the spectrophotometric method as shown in Fig. 7a for SrO and Fig. S5† for Ag_2O and CaO, respectively. The dye solution was degraded as a function of time and it was observed that as the time increased, the intensity of dye absorption was decreased in the presence of different photocatalysts. Fig. 7b shows the dye degradation over time and Fig. 7c and d present the percent of dye degradation efficiencies. The observed efficiencies of dye degradation were found to be 72%, 66% and 43% in the presence of SrO, Ag_2O and CaO photocatalysts, respectively, after 120 min of visible light irradiation, whereas the $Ag_2O{\cdot}SrO{\cdot}CaO$ nanocomposite showed 100% dye degradation efficiency under the same experimental conditions (Fig. 7d). As a result, it can be evidenced that the percent efficiencies of dye degradation in the presence of a ternary metal oxide nanocomposite is higher than those in the presence of single metal oxide nanocomposites. The binary/ternary catalysts are particularly preferred in the field of photocatalysis because of their enhanced photocatalytic properties and great advantages over monometallic counterparts.[21,50,54,65] The mixing of oxides can enhance the

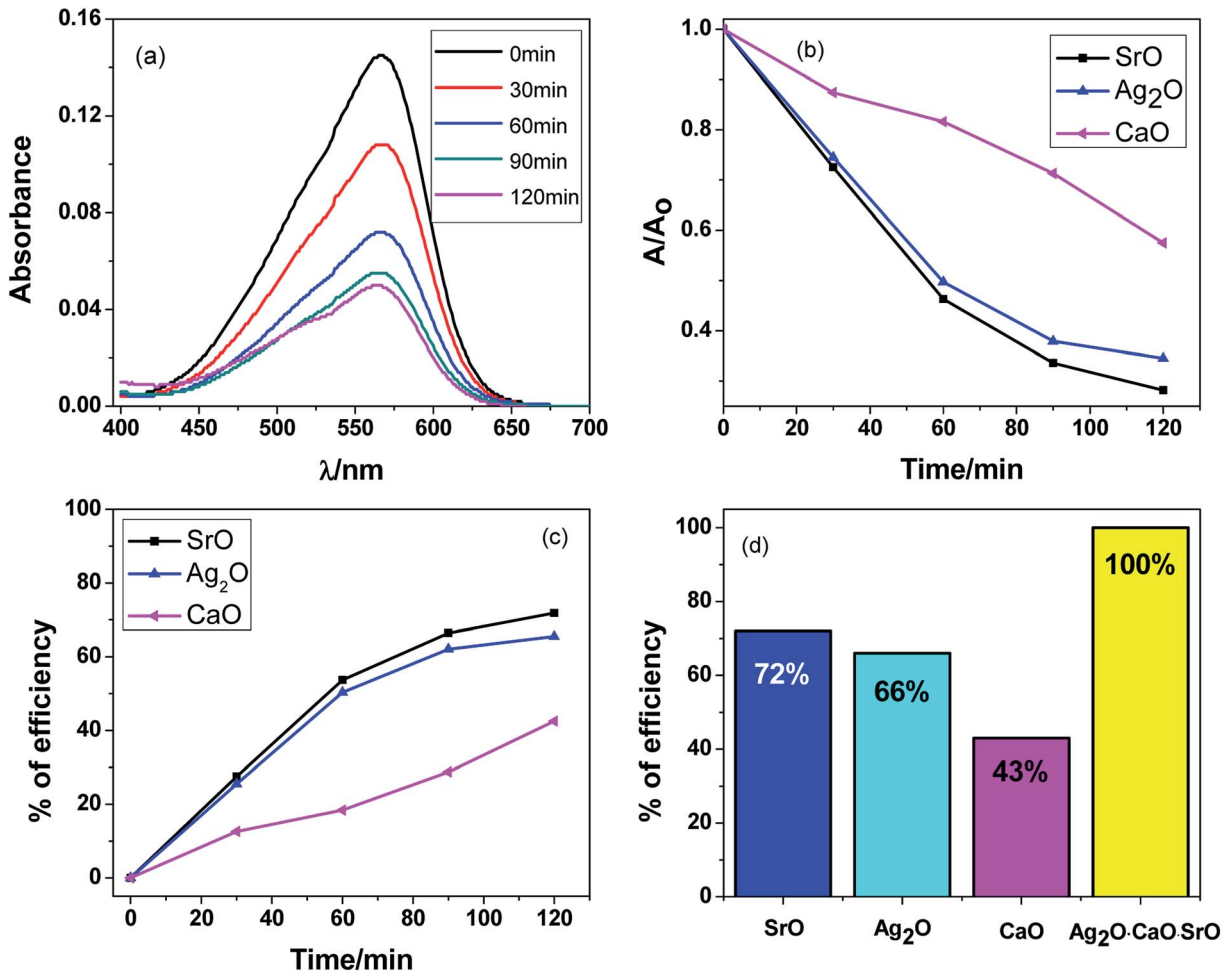

Fig. 7 Photocatalytic degradation of MV dye at pH 9 under visible light irradiation for 120 minutes with 30 minute time intervals in the presence of (a) SrO catalyst, (b) degradation of dye over time in the presence of SrO, Ag_2O and CaO catalysts, (c) % efficiency of dye degradation for SrO, Ag_2O and CaO over time and (d) comparison of % efficiency of dye degradation for SrO, Ag_2O, CaO and $Ag_2O{\cdot}SrO{\cdot}CaO$.

photocatalytic activity through the perturbation of energy levels in mixed metallic systems. The additional energy levels can act as a sink for the photogenerated electrons and eventually reduce the electron–hole recombination rate. In our previous studies, we used UV light for the catalytic degradation of dyes in the presence of a catalytic amount of H_2O_2 whereas in the current study, the catalyst alone was adequate to perform the photocatalytic degradation of MV dyes under visible light.

4.8. Appraisal of catalytic stability of the $Ag_2O{\cdot}SrO{\cdot}CaO$ nanocomposite

In order to investigate the stability of the $Ag_2O{\cdot}SrO{\cdot}CaO$ heterostructures under visible light irradiation, the same samples were recycled four times after separation by centrifugation, and the results are shown in Fig. 8a–d and S6.† Fig. 8a shows the decrease in absorption intensity of MV dye over time for the 1st cycle and Fig. S6a–d† show the change in the absorption intensities for the 2nd to 5th cycles. Fig. 8b shows the dye degradation over time for the 1st to 5th cycles and Fig. 8c indicates the percent efficiencies for the 1st to 5th cycles. The stability of $Ag_2O{\cdot}SrO{\cdot}CaO$ at pH 9 was evaluated by recycling experiments. In the photocatalytic process, the reclamation and reuse are important because of their contribution to lowering the maintenance cost of wastewater treatments and other processes. A simple procedure was followed to regenerate the photocatalyst. After completing the reaction, the solution was left standing for 24 h. The catalyst was thoroughly washed with acetone using a sonicator and then dried in open air. The stability of the catalyst was checked by reusing it several times. Similar conditions were used for each new cycle and the photocatalyst was reused for the degradation of a fresh MV solution after the photocatalyst was cleaned and dried. The percentage efficiencies were found to be 100%, 92%, 90%, 85% and 83% at pH 9 after five cycles (Fig. 8d). The remaining photocatalytic efficiency obtained in the five-cycle reusability tests demonstrated the promising application potential of $Ag_2O{\cdot}SrO{\cdot}CaO$ nanoparticles as a photocatalyst. The results showed that the photocatalytic activity decreased after each cycle and this decrease in the photocatalytic activity of the catalyst may be due to the absorption of intermediate products on the active sites of the catalyst and the structural changes of the photocatalyst after

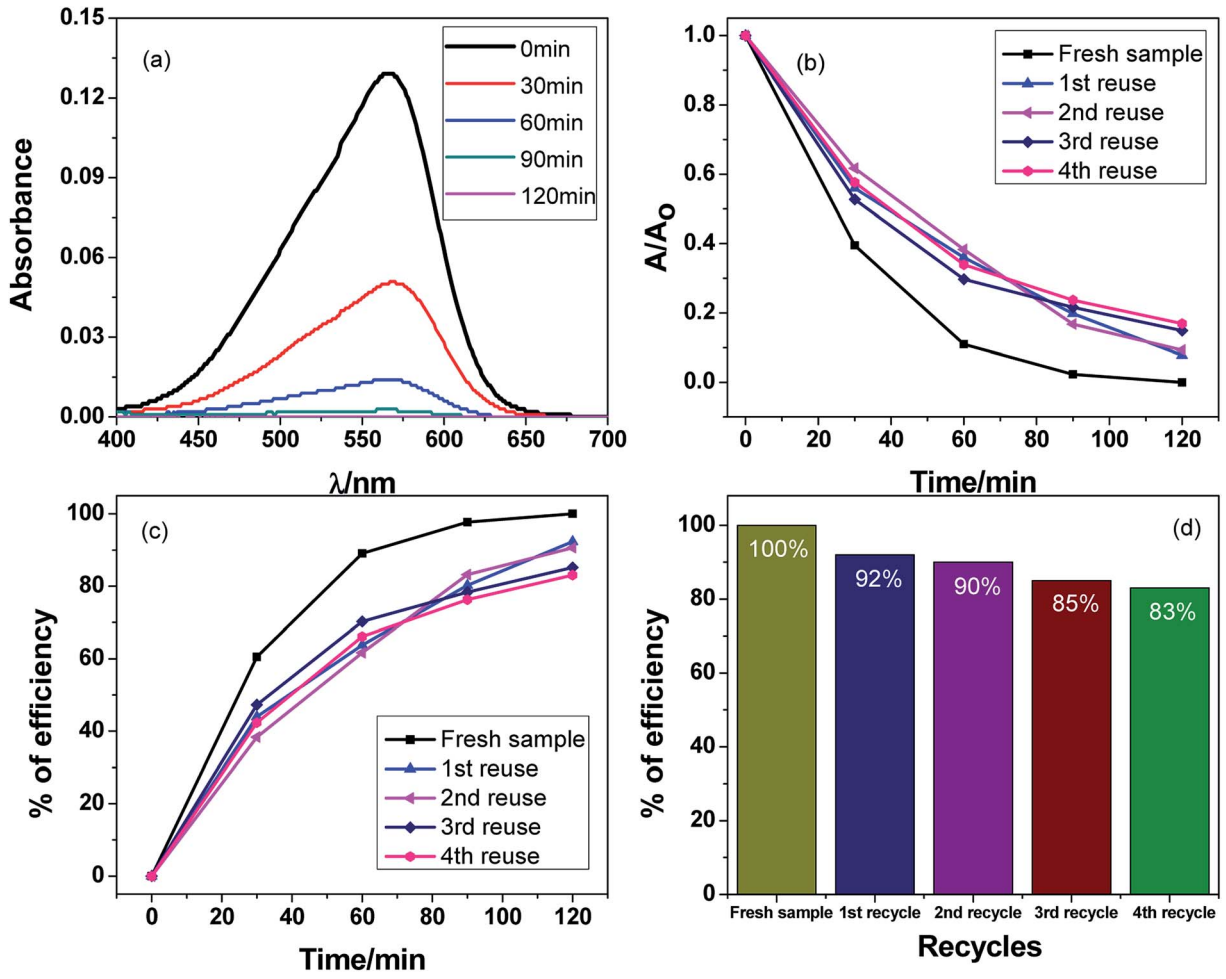

Fig. 8 Recycle and reuse of the $Ag_2O{\cdot}SrO{\cdot}CaO$ photocatalyst for MV dye degradation (MV concentration: 0.0393 g L^{-1}; photocatalyst dosage: 0.05 g L^{-1}) in the presence of catalyst at pH 9 (a) decrease in absorption from 1st cycle, (b) dye degradation over time, (c) percent efficiency over time and (d) % efficiency of catalyst for 1st to 5th cycle.

Table 1 Antibacterial activities of $Ag_2O{\cdot}SrO{\cdot}CaO$ nanocomposite against pathogenic bacteria in the dark

	Diameter of inhibition zone, D_{iz} (mm)				Ratio, $R = D_{iz}/D_w$		
Bacterial culture	1	2	3	Diameter of well, D_w (mm)	1	2	3
Serratia marcescens	0	0	30	4	0	0	7.5
Klebsiella pneumoniae	0	0	31	4	0	0	7.75
Bacillus subtilis	0	0	29	4	0	0	7.25
Staphylococcus aureus	0	0	30	4	0	0	7.5
Pseudomonas aeruginosa	0	0	31	4	0	0	7.75
Escherichia coli	0	0	31	4	0	0	7.75
Proteus mirabilis	0	0	21	4	0	0	5.25

reuse for several times. However, another reason for the decrease in the catalytic activity may be the loss of some quantity of the catalyst during the filtration process.

4.9. Antibacterial activity of $Ag_2O{\cdot}SrO{\cdot}CaO$ nanoparticles

Mixed metal oxide nanoparticles are being thoroughly investigated as potential antibacterial agents. Moreover, the antibacterial activity varies with particle size[66] and the antibacterial effect is also affected by different morphologies and crystal growth behaviors.[67] The antibacterial activity of the mixed metal oxide nanocomposite, $Ag_2O{\cdot}SrO{\cdot}CaO$, was tested against some pathogenic bacteria including Gram-positive (*S. aureus*, *B. subtilis*) and Gram-negative bacteria (*S. marcescens*, *E. coli*, *K. pneumoniae*, *P. aeruginosa*, *P. mirabilis*) by the agar well diffusion method in the absence and presence of visible light. The obtained results are shown in Tables 1 and 2. The pathogenic bacterial isolates were precultured in nutrient broth media at 37 °C for 120 rpm and were held overnight. The mixed metal oxide nanocomposite samples were prepared as 1 mg mL^{-1}, 2 mg mL^{-1}, and 3 mg mL^{-1}. Müller–Hinton agar nutrients were used for the subculture of the pure cultures of organisms. A ~4 mm depth well was created on the agar media and about 60 μL of solution was poured in each well from the prepared nanocomposite solutions using a micropipette. Cotrimoxazole (COT 25) was used as a control. The plates were incubated at 37 °C for almost 24 h and then the different levels of zone inhibition were measured. From the clear zone of inhibition (as shown in Fig. 9 and 10), it was found that in the dark, the $Ag_2O{\cdot}SrO{\cdot}CaO$ nanocomposite showed antibacterial effects in the case of solution 3 only by killing both Gram-positive and Gram-negative bacteria. However, in the presence of light, all the three solutions of different concentrations showed antibacterial activity, albeit a widely varying degree. This is because of the excitation of the composite by light and formation of the radicals like reactive oxygen species (ROS) in solution, which facilitate the enhancement of bacteria killing through the ROS mechanism. Thus, the nanostructured $Ag_2O{\cdot}SrO{\cdot}CaO$ composite affords great mechanical damage to the cell wall and the functions of bacteria as well as an enhanced bactericidal effect.

4.10. Determination of MIC and MBC

The minimal inhibitory concentration (MIC) is defined as the lowest concentration of a compound that will completely inhibit the visible growth of microorganisms after an overnight incubation. In this study, the microdilution method was employed to evaluate the MIC of the $Ag_2O{\cdot}SrO{\cdot}CaO$ nanocomposite against two Gram-positive and five Gram-negative bacteria (as shown in Fig. 11). At first, all the pathogenic bacterial cultures were grown in nutrient broth (0.5% NaCl, 0.5% peptone, 0.15% beef extract, 0.15% yeast extract: pH 7) overnight at 37 °C in a shaker incubator (120 rpm). Then, a series of $Ag_2O{\cdot}SrO{\cdot}CaO$ nanocomposite solutions (1 μg μL^{-1}, 0.5 μg μL^{-1}, 0.25 μg μL^{-1}, 0.13 μg μL^{-1}, 0.065 μg μL^{-1}, 0.032 μg μL^{-1}, 0.016 μg μL^{-1}, 0.008 μg μL^{-1} and 0.004 μg μL^{-1}) were

Table 2 Antibacterial activities of the $Ag_2O{\cdot}SrO{\cdot}CaO$ nanocomposite against pathogenic bacteria in the presence of visible light

	Diameter of inhibition zone, D_{iz} (mm)				Ratio, $R = D_{iz}/D_w$		
Bacterial culture	1	2	3	Diameter of well, D_w (mm)	1	2	3
Serratia marcescens	28	28	31	4	7	7	7.75
Klebsiella pneumoniae	28	29	35	4	7	7.25	8.75
Bacillus subtilis	26	27	30	4	6	6.75	7.5
Staphylococcus aureus	30	32	33	4	7.5	8	8.25
Pseudomonas aeruginosa	30	30	33	4	7.5	7.5	8.25
Escherichia coli	29	30	32	4	7.25	7.5	8
Proteus mirabilis	18	18	22	4	4.5	4.5	5.5

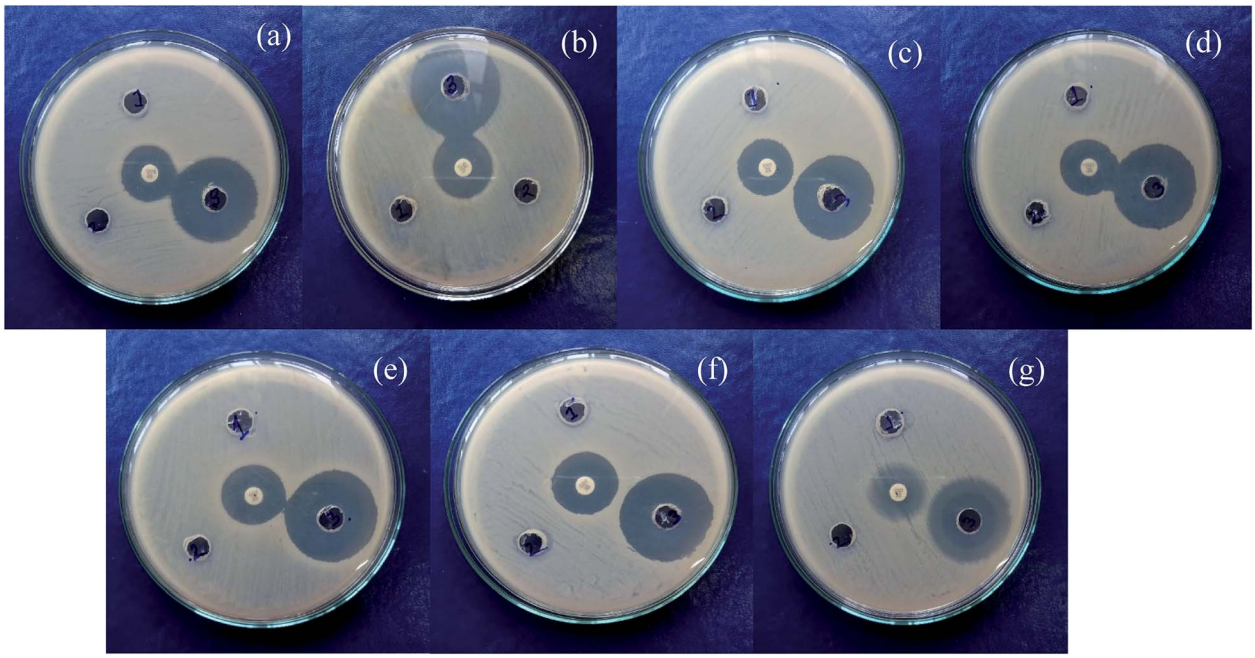

Fig. 9 Antibacterial activities of $Ag_2O{\cdot}SrO{\cdot}CaO$ nanocomposite in the dark with different concentrations of solutions as (1) 1 mg mL^{-1}, (2) 2 mg mL^{-1} and (3) 3 mg mL^{-1} in the presence of (a) *Serratia marcescens*, (b) *Klebsiella pneumoniae*, (c) *Bacillus subtilis*, (d) *Staphylococcus aureus*, (e) *Pseudomonas aeruginosa*, (f) *Escherichia coli* and (g) *Proteus mirabilis* (middle spot is for the control, COT 25).

prepared using a 2-fold serial dilution method in the microtiter plate. Then, 100 μL of bacterial suspension was added in the respective well containing $Ag_2O{\cdot}SrO{\cdot}CaO$ nanocomposite solution according to the Mac Farland standard 0.5 and incubated at 37 °C for 24 h. After a 24 h incubation, 20 μL of Presto Blue was added in each well and further incubated at 37 °C for 2–4 h. A change in color from blue to pink indicated the growth of bacteria *via* the reduction of resazurin, and the MIC was defined as the lowest concentration of the $Ag_2O{\cdot}SrO{\cdot}CaO$ solution that prevented this change in color. A change in the

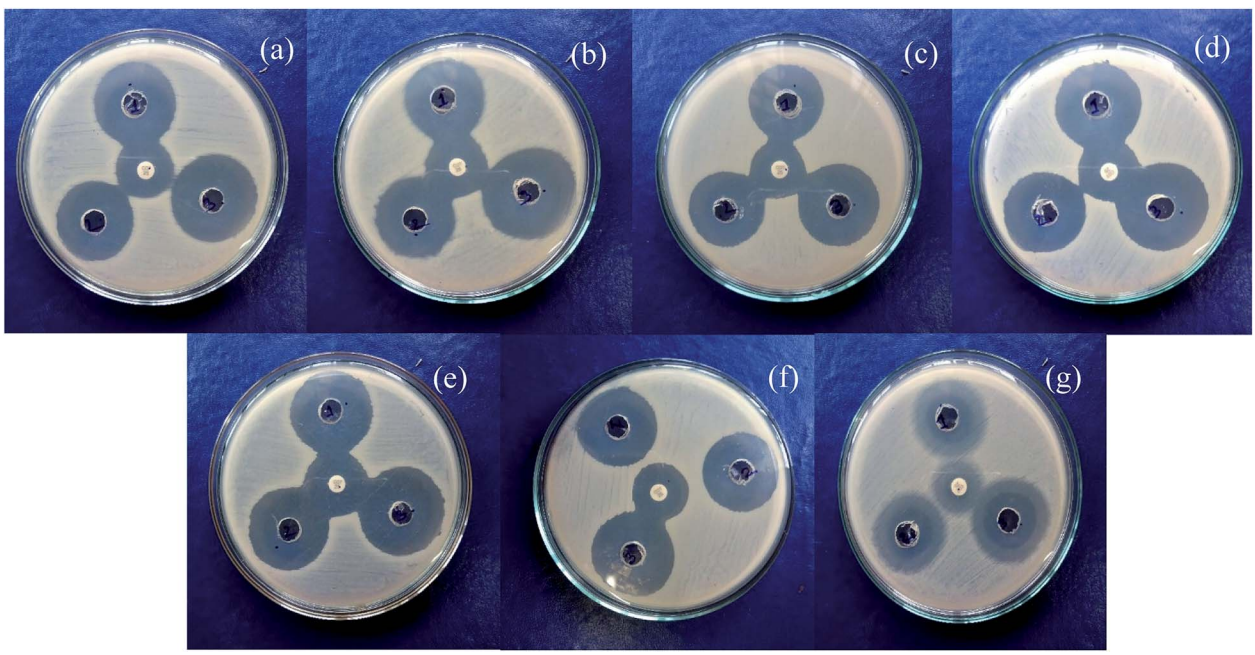

Fig. 10 Antibacterial activities of $Ag_2O{\cdot}SrO{\cdot}CaO$ nanocomposite in the presence of visible light with different concentrations of solutions as (1) 1 mg mL^{-1}, (2) 2 mg mL^{-1} and (3) 3 mg mL^{-1} in the presence of (a) *Serratia marcescens*, (b) *Klebsiella pneumoniae*, (c) *Bacillus subtilis*, (d) *Staphylococcus aureus*, (e) *Pseudomonas aeruginosa*, (f) *Escherichia coli* and (g) *Proteus mirabilis* (middle spot is for the control, COT 25).

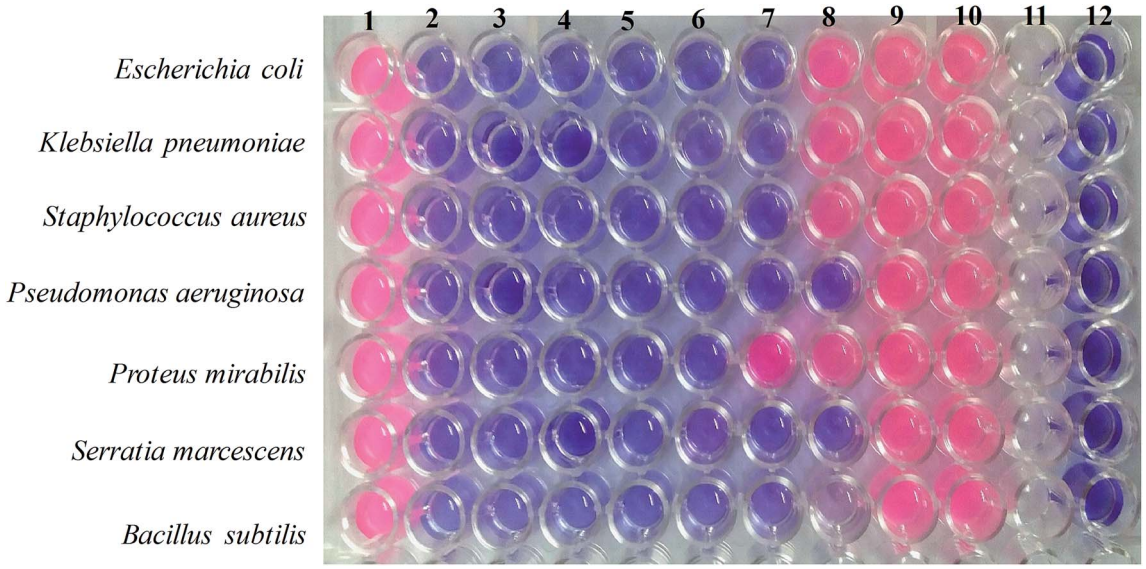

Fig. 11 Determination of MIC and MBC values for the $Ag_2O{\cdot}SrO{\cdot}CaO$ nanocomposite against some pathogenic bacteria including Gram-positive (*S.aureus, B. subtilis*) and Gram-negative bacteria (*S. marcescens, E. coli, K. pneumoniae, P. aeruginosa, P. mirabilis*).

color of the growth control well to pink indicated the proper growth of the isolate and no change in the color of the sterile control well indicated the absence of contaminants (Fig. 11, column 1 and 12 respectively).

The minimum bactericidal concentration (MBC) was determined by directly plating the content of wells with concentrations higher than the MIC value, as detailed in Table 3. The MBC value was determined when there was no colony growth from the directly plated contents of the wells. Thus, the MIC and MBC values indicated the effective dose of $Ag_2O{\cdot}SrO{\cdot}CaO$ against different Gram-positive and Gram-negative bacteria.

4.11. Electrochemical application with $Ag_2O{\cdot}SrO{\cdot}CaO$ nanomaterials/GCE sensor probe. The working electrode of the sensor was fabricated by the deposition of $Ag_2O{\cdot}SrO{\cdot}CaO$ nanomaterials on a GCE as a thin film of nanoparticles and the long-term stability of the deposited thin film of NPs was enhanced by the addition of a drop of 5% Nafion suspension. The Nafion is a copolymer and it has its own conductivity. As a result, the electron transfer rate as well as the conductivity of the working electrode is increased due to the use of Nafion, as described in previous reports.[68–72] During the electrochemical detection of 3-CP in PBS, the 3-CP molecules are adsorbed on the surface of the NPs of the modified GCE and by the influence of the applied potential, they are oxidized to CO_2, H^+, and free electrons. The generated free electrons trigger the high conductivity of the sensing buffer phase and amplified *I–V* responses are recorded in the Keithley electrometer. The electrochemical oxidation of 3-CP has been described by earlier authors.[73,74] The proposed electrochemical reaction is shown in eqn (i)

$$C_6OH_5Cl + 11H_2O \rightarrow 6CO_2 + 27H^+ + Cl^- + 26e^- \quad \text{(i)}$$

A pictorial representation of the electrochemical oxidation of 3-CP is shown in Scheme 1.

At the onset of this study, chemicals that are environmentally toxic were analyzed in the electrochemical (*I–V*) approach in a buffer phase. Fig. 12a shows the electrochemical responses of DEM, 3-MA, 3-MP, 2,4-DAPDHCl, 3-MPHydHCl, benzaldehyde, *m*-THydHCl, 3-CP, 4-MP and zimtaldehyde. The experiment was executed using 0.1 μM of each toxin in PBS. From Fig. 12a, it is clear that 3-CP shows the highest *I–V* responses and based on this, 3-CP is nominated as the selective toxin for the assembled sensor composed of the $Ag_2O{\cdot}SrO{\cdot}CaO$ nanomaterials/GCE. Then, 3-CP was subjected to the *I–V* analysis corresponding to the concentration of 0.1 nM to 0.1 mM, as illustrated in Fig. 12b. Fig. 12b shows that the electrochemical (*I–V*) responses are distinguished from a lower to higher concentration and can be separated from one to another. Thus, the *I–V* responses are varied with the concentration of 3-CP, which is similar to observations in previous articles detecting various environmental toxins with the *I–V* approach.[75–79] A calibration plot of the current *versus* concentration of 3-CP was executed, as illustrated in Fig. 12c. For this exploration, the current data are separated in Fig. 12b at a potential of +1.5 V. As

Table 3 Determination of MIC and MBC by the Presto Blue aided microdilution method of the $Ag_2O{\cdot}SrO{\cdot}CaO$ nanocomposite against seven pathogenic bacteria

Bacteria	MIC reported in this study (μg mL^{-1})	MBC reported in this study (μg mL^{-1})
Escherichia coli	0.032	0.065
Klebsiella pneumoniae	0.032	0.065
Staphylococcus aureus	0.032	0.065
Pseudomonas aeruginosa	0.016	0.032
Proteus mirabilis	0.065	0.125
Serratia marcescens	0.016	0.032
Bacillus subtilis	0.016	0.032

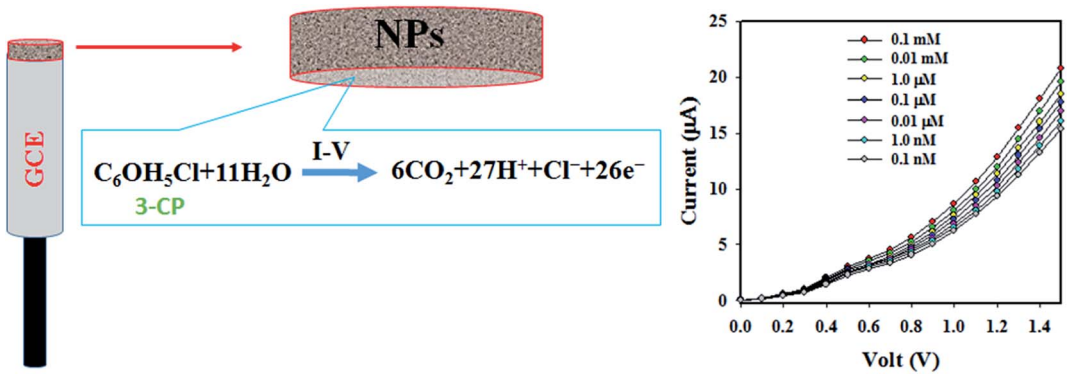

Scheme 1 Electrochemical detection mechanism of 3-CP in the buffer phase.

shown in Fig. 12c, the current data are linearly distributed corresponding to the concentration range of 0.1 nM to 0.01 mM, which provides evidence for the reliability of this method and the range of concentration is defined as the LDR. Obviously, the resulting LDR is a wider range of concentration. To examine the linearity of the LDR, a plot of the current *versus* log (conc. of 3-

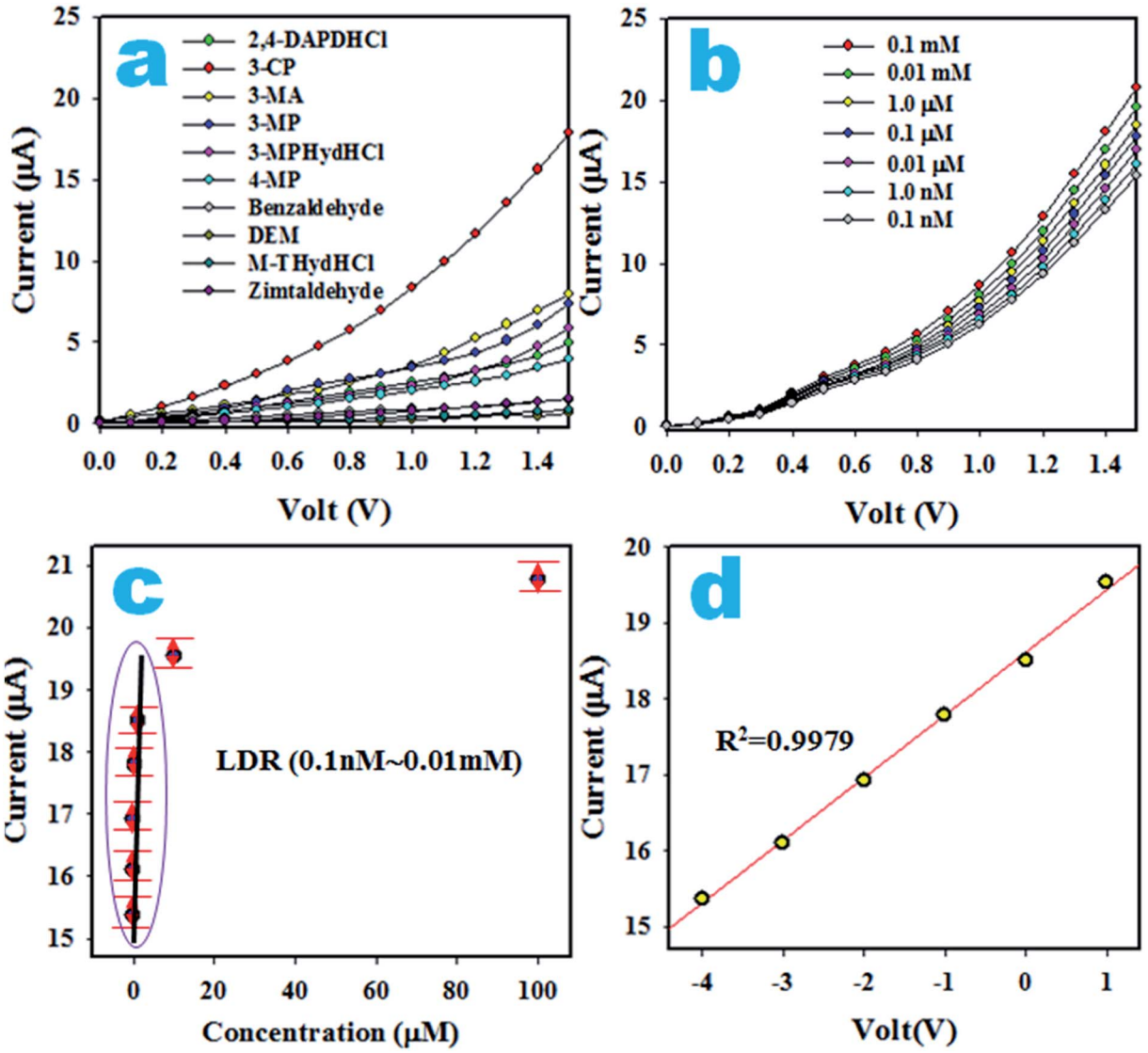

Fig. 12 The electrochemical evaluation of the sensor based on $Ag_2O \cdot SrO \cdot CaO$ nanomaterials/GCE. (a) The tests for selectivity, (b) *I*–*V* responses of 3-CP based on concentration, (c) current *versus* log (concentration) and (d) calibration of 3-CP sensor.

CP) was created, as shown in Fig. 12d, which is close-fitted with the regression co-efficient $R^2 = 0.9979$, showing the high linearity of the LDR. From the slope of the calibration curve, the sensor sensitivity is calculated, 8.9684 μA μM^{-1} cm^{-2}, which is an appreciable outcome. Using a signal-to-noise ratio of 3, the lower limit is detected, 97.12 ± 4.86 pM, which is a considerably lower limit for the detection of 3-CP in a buffer medium.

The response time is an efficiency measuring parameter of a sensor and is defined as the time it takes to complete a *I–V* investigation of an analyte. To determine the response time, 0.1 μM 3-CP was analyzed by the assembled sensor with $Ag_2O{\cdot}SrO{\cdot}CaO$ nanomaterials/GCE and the resulting data is plotted as the current *versus* time (s), as illustrated in Fig. 13a. An appreciable response time around 30.0 s is observed. A comparison of the *I–V* responses in the analysis of 3-CP with GCE and coated GCE are presented in Fig. 13b and it is shown that the coated GCE has the maximum potential for the detection of 3-CP. Fig. 13c shows the reproducibility of the 3-CP sensor with $Ag_2O{\cdot}SrO{\cdot}CaO$ nanomaterials/GCE. The reproducibility describes the capability of the sensor to produce similar results under similar conditions.

As shown in Fig. 13c, the seven *I–V* outcomes in the detection of 3-CP at 0.1 μM and potential 0 to +1.5 V in a buffer phase in seven successive hours are completely identical and cannot be distinguished. The deviation from idleness is not perceived even after washing the electrode after each analysis. Then, the precision of the reproducibility, the relative standard deviation (RSD), was measured and found to be 1.41%. Thus, the reproducibility parameter shows us that the 3-CP sensor is reliable. The stability of the proposed 3-CP sensor in a buffer phase is necessary and it was tested by the execution of the reproducibility parameter for seven continual days, as illustrated in

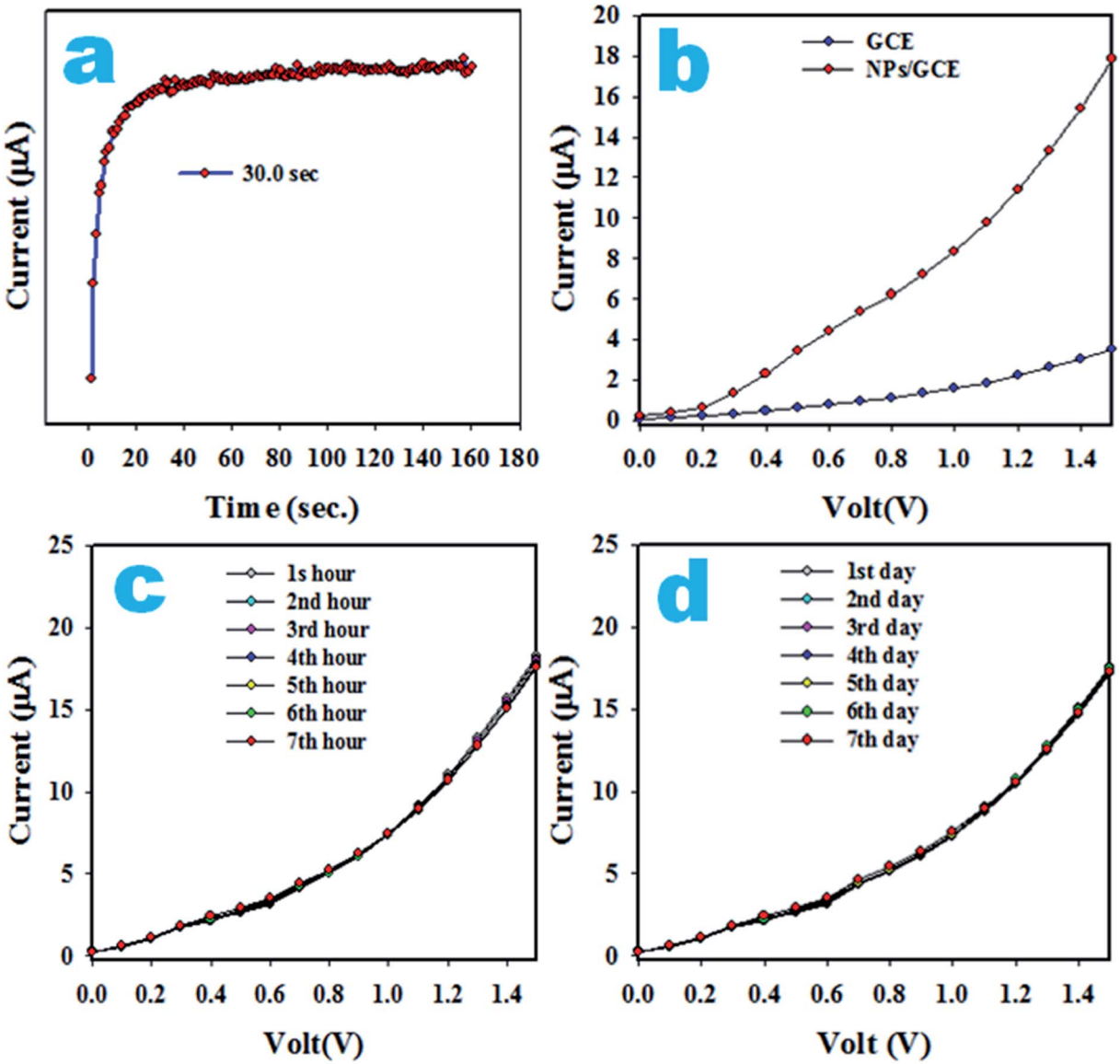

Fig. 13 Optimization: (a) response time, (b) comparison of *I–V* responses in the detection of 3-CP, (c) reproducibility and (d) long-time stability measurement.

Table 4 The performance of earlier invented 3-CP chemical sensors[a]

Modified GCE	Analyte	DL	LDR	Sensitivity	Ref.
MCM-41 NMs/GCE	1,2-DCB	13.0 pM	0.089 nM to 8.9 mM	0.7468 μA μM^{-1} cm^{-2}	80
Ag@Nd_2O_3 NPs/GCE	4-NP	0.43 pM	1.0 pM to 0.1 mM	0.221 μA μM^{-1} cm^{-2}	81
Fe_3O_4@Ag@Ni NMs/GCE	2,4-DAP	5.4 pM	0.1 nM to 1.0 mM	3.5217 μA μM^{-1} cm^{-2}	82
Ag_2O·SrO·CaO nanomaterials/GCE	3-CP	97.12 pM	0.1 nM to 0.01 mM	8.9684 μA μM^{-1} cm^{-2}	This work

[a] DL, detection limit; LDR, linear dynamic range; nM, nanomole; μM, micromole; pM, picomole.

Table 5 The analysis of environmental samples using Ag_2O·SrO·CaO nanomaterials/GCE sensor by recovery method

Sample	Added 3-CP concentration (μM)	Measured 3-CP conc.[a] by Ag_2O·SrO·CaO nanomaterials/GCE (μM)			Average recovery[b] (%)	RSD[c] (%) ($n = 3$)
		R1	R2	R3		
Sea water	0.01000	0.0091	0.00982	0.00983	98.28	0.10
PC-water bottle	0.01000	0.0091	0.00982	0.00967	98.01	1.24
Tap water	0.01000	0.0096	0.00962	0.00968	95.59	1.19

[a] Mean of three repeated determination (signal to noise ratio 3) Ag_2O·SrO·CaO nanomaterials/GCE. [b] Concentration of 3-CP determined/concentration taken (unit: nM). [c] Relative standard deviation value indicates precision among three repeated measurements (R1, R2, R3).

Fig. 13d. The stability showed an outcome similar to the reproducibility. It can be summarized that the proposed 3-CP sensor is well-suited for detecting 3-CP in a buffer solution. For further validity, a comparison of similar studies is highlighted in Table 4 in terms of the analytical parameters, such as sensitivity, LDR and DL.[80–82] Based on the explored data, the 3-CP sensor with the Ag_2O·SrO·CaO nanomaterials/GCE exhibits the best performance.

4.12. Analysis of real samples. To establish the effectiveness of the 3-CP sensor based on the Ag_2O·SrO·CaO nanomaterials/GCE, it was subjected to the detection of 3-CP in real samples collected from environmental sources using a recovery method illustrated in Table 5. The resulting data are represented in Table 5 and it seems to be quite satisfactory.

5. Conclusion

A Ag_2O·SrO·CaO multi-metal oxide nanocomposite was synthesized by a facile co-precipitation method following calcination for 5 h at 600 °C. The synthesized nanocomposite was characterized by XRD, FESEM, EDS, TEM, FTIR and PL spectroscopy. The Ag_2O·SrO·CaO heterostructure nanocomposite demonstrates exemplary photocatalytic activity under visible light irradiation. From the results of the MV dye degradation, it was found that the percent efficiency of dye degradation was much greater for the multi-metal oxide nanocomposite than for the corresponding single metal oxides. The Ag_2O·SrO·CaO nanocomposite showed excellent photocatalytic activity and exhibited 100%, 57% and 31% degradation efficiency under a visible light irradiation at pH 9, 7 and 4, respectively, within 120 minutes, whereas the efficiencies of dye degradation were found to be 72%, 66% and 43% in the presence of SrO, Ag_2O and CaO photocatalysts, respectively, at pH 9 after 120 min of visible light irradiation. Thus, the Ag_2O·SrO·CaO mixed metal oxide nanocomposite is an excellent photocatalyst due to its dye removal ability and reusability. It also showed enhanced antibacterial activities against some Gram-positive and Gram-negative pathogenic bacteria in the absence and presence of visible light. In the presence of light, the anti-bacterial activities were found to be boosted up remarkably because of the formation of ROS. The MIC and MBC value of the Ag_2O·SrO·CaO nanocomposite were also determined against these pathogenic bacteria, which indicated the minimum dose for effective anti-bacterial functions. The 3-CP sensor with Ag_2O·SrO·CaO nanomaterials/GCE was investigated in detail to evaluate the sensitivity, LDR and detection limit, which were appreciable. It was examined for reproducibility, response time and long-term stability, which were also outstanding. Finally, the validation of this sensor was executed to detect 3-CP in real environmental samples by applying the recovery method and it was found to be reliable.

Conflicts of interest

There are no conflicts to declare.

Acknowledgements

Md Abdus Subhan acknowledged Fulbright USA for Visiting Scholar Award 2018–19 at Northeastern University, Boston, MA, USA. Professor Dr Piyasan Praserthdam of Chulalongkorn University, Bangkok, Thailand is acknowledged for his cooperation in XRD study. Dr William Ghann and Dr Hyeonggon Kang of Coppin State University, USA are acknowledged for recording

FESEM and TEM images respectively. SUST Research Grant No. PS/2019/106 is acknowledged for funding. Center of Excellence for Advanced Materials Research (CEAMR), King Abdulaziz University, Jeddah, Saudi Arabia is highly acknowledged for their lab facilities and instrumental supports.

References

1 P. N. Kapoor, A. K. Bhagi, R. S. Mulukutla and K. J. Klabunde, Mixed metal oxide nanoparticles, *Dekker Encycl. Nanosci. Nanotechnol.*, 2004, 2007–2015.

2 J. A. Rodriguez and D. Stacchiola, Catalysis and the nature of mixed-metal oxides at the nanometer level: special properties of MO_x/TiO_2 (110){M = V, W, Ce} surfaces, *Phys. Chem. Chem. Phys.*, 2010, **12**(33), 9557–9565.

3 K. R. Nemade and S. A. Waghuley, UV–VIS spectroscopic study of one pot synthesized strontium oxide quantum dots, *Results Phys.*, 2013, **3**, 52–54.

4 R. Jose, T. Suzuki and Y. Ohishi, Thermal and optical properties of TeO_2–BaO–SrO–Nb_2O_5 based glasses: new broadband Raman gain media, *J. Non-Cryst. Solids*, 2006, **352**(52–54), 5564–5571.

5 A. K. Ganguli, T. Ahmad, P. R. Arya and P. Jha, Nanoparticles of complex metal oxides synthesized using the reverse-micellar and polymeric precursor routes, *Pramana*, 2005, **65**(5), 937–947.

6 A. Verma and M. S. Mehata, Controllable synthesis of silver nanoparticles using neem leaves and their antimicrobial activity, *J. Radiat. Res. Appl. Sci.*, 2016, **9**(1), 109–115.

7 J. A. Spadaro, T. J. Berger, S. D. Barranco, S. E. Chapin and R. O. Becker, Antibacterial effects of silver electrodes with weak direct current, *Antimicrob. Agents Chemother.*, 1974, **6**(5), 637–642.

8 G. Zhao and S. E. Stevens, Multiple parameters for the comprehensive evaluation of the susceptibility of Escherichia coli to the silver ion, *BioMetals*, 1998, **11**(1), 27–32.

9 F. Derikvand, F. Bigi, R. Maggi, C. G. Piscopo and G. Sartori, Oxidation of hydroquinones to benzoquinones with hydrogen peroxide using catalytic amount of silver oxide under batch and continuous-flow conditions, *J. Catal.*, 2010, **271**(1), 99–103.

10 W. Wang, Q. Zhao, J. Dong and J. Li, A novel silver oxides oxygen evolving catalyst for water splitting, *Int. J. Hydrogen Energy*, 2011, **36**(13), 7374–7380.

11 E. Sanli, B. Z. Uysal and M. L. Aksu, The oxidation of $NaBH_4$ on electrochemicaly treated silver electrodes, *Int. J. Hydrogen Energy*, 2008, **33**(8), 2097–2104.

12 V. V. Petrov, T. N. Nazarova, A. N. Korolev and N. F. Kopilova, Thin sol–gel SiO_2–SnO_x–AgO_y films for low temperature ammonia gas sensor, *Sens. Actuators, B*, 2008, **133**(1), 291–295.

13 Y. Ida, S. Watase, T. Shinagawa, M. Watanabe, M. Chigane, M. Inaba and M. Izaki, Direct electrodeposition of 1.46 eV bandgap silver (I) oxide semiconductor films by electrogenerated acid, *Chem. Mater.*, 2008, **20**(4), 1254–1256.

14 W. X. Li, C. Stampfl and M. Scheffler, Insights into the function of silver as an oxidation catalyst by ab initio atomistic thermodynamics, *Phys. Rev. B*, 2003, **68**(16), 165412.

15 Y. H. Wang and H. Y. Gu, Hemoglobin co-immobilized with silver–silver oxide nanoparticles on a bare silver electrode for hydrogen peroxide electroanalysis, *Microchim. Acta*, 2009, **164**(1–2), 41–47.

16 C. Ngamcharussrivichai, W. Meechan, A. Ketcong, K. Kangwansaichon and S. Butnark, Preparation of heterogeneous catalysts from limestone for transesterification of vegetable oils—Effects of binder addition, *J. Ind. Eng. Chem.*, 2011, **17**(3), 587–595.

17 M. Amin Alavi and A. Morsali, Ultrasonic-assisted synthesis of $Ca(OH)_2$ and CaO nanostructures, *J. Exp. Nanosci.*, 2010, **5**(2), 93–105.

18 M. M. Ostromecki, L. J. Burcham and I. E. Wachs, The influence of metal oxide additives on the molecular structures of surface tungsten oxide species on alumina. II. In situ conditions, *J. Mol. Catal. A: Chem.*, 1998, **132**(1), 59–71.

19 A. Roy and J. Bhattacharya, Microwave-assisted synthesis and characterization of CaO nanoparticles, *Int. J. Nanosci.*, 2011, **10**(03), 413–418.

20 Y. Zhu, S. Wu and X. Wang, Nano CaO grain characteristics and growth model under calcination, *Chem. Eng. J.*, 2011, **175**, 512–518.

21 M. A. Subhan, P. C. Saha, M. M. Alam, A. M. Asiri, M. Al-Mamun and M. M. Rahman, Development of Bis-Phenol A sensor based on $Fe_2MoO_4 \cdot Fe_3O_4 \cdot ZnO$ nanoparticles for sustainable environment, *J. Environ. Chem. Eng.*, 2018, **6**(1), 1396–1403.

22 S. Assabumrungrat, P. Sonthisanga, W. Kiatkittipong, N. Laosiripojana, A. Arpornwichanop, A. Soottitantawat and P. Praserthdam, Thermodynamic analysis of calcium oxide assisted hydrogen production from biogas, *J. Ind. Eng. Chem.*, 2010, **16**(5), 785–789.

23 T. Liu, Y. Zhu, X. Zhang, T. Zhang, T. Zhang and X. Li, Synthesis and characterization of calcium hydroxide nanoparticles by hydrogen plasma-metal reaction method, *Mater. Lett.*, 2010, **64**(23), 2575–2577.

24 N. A. Oladoja, I. A. Ololade, S. E. Olaseni, V. O. Olatujoye, O. S. Jegede and A. O. Agunloye, Synthesis of nano calcium oxide from a gastropod shell and the performance evaluation for Cr (VI) removal from aqua system, *Ind. Eng. Chem. Res.*, 2012, **51**(2), 639–648.

25 R. Sengodan, R. Ranjithkumar, K. Selvam and B. Chandarshekar, Antibacterial Activity Of Silver Nanoparticles Coated Intravascular Catheters (Agnps-Ivc) Against Biofilm Producing Pathogens, *Rasayan J. Chem.*, 2018, **11**(1), 63–68.

26 F. S. Kodeh, I. M. El-Nahhal, E. A. Elkhair and A. H. Darwish, Synthesis of CaO–Ag-NPs@ $CaCO_3$ Nanocomposite via Impregnation of Aqueous Sol Ag-NPs onto Calcined Calcium Oxalate, *Chem. Afr.*, 2019, 1–8.

27 M. Ambrosi, L. Dei, R. Giorgi, C. Neto and P. Baglioni, Colloidal particles of $Ca(OH)_2$: properties and applications to restoration of frescoes, *Langmuir*, 2001, **17**(14), 4251–4255.
28 M. Dürr, S. Rosselli, A. Yasuda and G. Nelles, Band-gap engineering of metal oxides for dye-sensitized solar cells, *J. Phys. Chem. B*, 2006, **110**(43), 21899–21902.
29 L. L. Beecroft and C. K. Ober, Novel ceramic particle synthesis for optical applications: dispersion polymerized preceramic polymers as size templates for fine ceramic powders, *Adv. Mater.*, 1995, **7**(12), 1009–1012.
30 A. Taden, M. Antonietti, A. Heilig and K. Landfester, Inorganic films from three different phosphors via a liquid coating route from inverse miniemulsions, *Chem. Mater.*, 2004, **16**(24), 5081–5087.
31 X. Y. Zhang, T. W. Wang, W. Q. Jiang, D. Wu, L. Liu and A. H. Duan, Preparation and characterization of three-dimensionally ordered crystalline microporous CeO_2, *Chin. Chem. Lett.*, 2005, **16**(8), 1109.
32 J. Lu, Z. Tang, Z. Zhang and W. Shen, Preparation of $LiFePO_4$ with inverse opal structure and its satisfactory electrochemical properties, *Mater. Res. Bull.*, 2005, **40**(12), 2039–2046.
33 G. Gundiah, and C. N. R. Rao, Macroporous oxide materials with three-dimensionally interconnected pores, *Advances In Chemistry: A Selection of CNR Rao's Publications (1994–2003)*, 2003, pp. 459–464.
34 J. Michalowicz and W. Duda, Phenols-sources and toxicity, *Pol. J. Environ. Stud.*, 2007, **16**(3), 347–362.
35 R. H. AL-Ammari, A. A. Ganash and M. A. Salam, Electrochemical molecularly imprinted polymer based on zinc oxide/graphene/poly (o-phenylenediamine) for 4-chlorophenol detection, *Synth. Met.*, 2019, **254**, 141–152.
36 C. Wang, Y. Zhao, L. Xu, P. Yan, J. Qian, L. Zhao and H. Li, Specific electron-transfer and surface plasmon resonance integrated boosting visible-light photoelectrochemical sensor for 4-chlorophenol, *J. Electroanal. Chem.*, 2019, **833**, 251–257.
37 M. Wei, D. Tian, S. Liu, X. Zheng, S. Duan and C. Zhou, β-Cyclodextrin functionalized graphene material: a novel electrochemical sensor for simultaneous determination of 2-chlorophenol and 3-chlorophenol, *Sens. Actuators, B*, 2014, **195**, 452–458.
38 M. Czaplicka, Sources and transformations of chlorophenols in the natural environment, *Sci. Total Environ.*, 2004, **322**(1–3), 21–39.
39 D. A. Haines, G. Saravanabhavan, K. Werry and C. Khoury, An overview of human biomonitoring of environmental chemicals in the Canadian Health Measures Survey: 2007–2019, *Int. J. Hyg. Environ. Health*, 2017, **220**(2), 13–28.
40 J. De Coster, W. Vanherck, L. Appels and R. Dewil, Selective electrochemical degradation of 4-chlorophenol at a Ti/RuO_2-IrO_2 anode in chloride rich wastewater, *J. Environ. Manage.*, 2017, **190**, 61–71.
41 J. Li, X. Li, R. Yang, L. Qu and P. D. B. Harrington, A sensitive electrochemical chlorophenols sensor based on nanocomposite of ZnSe quantum dots and cetyltrimethylammonium bromide, *Anal. Chim. Acta*, 2013, **804**, 76–83.
42 B. Wang, O. K. Okoth, K. Yan and J. Zhang, A highly selective electrochemical sensor for 4-chlorophenol determination based on molecularly imprinted polymer and PDDA-functionalized graphene, *Sens. Actuators, B*, 2016, **236**, 294–303.
43 R. A. Abuknesha and H. M. Griffith, Evaluation of a polyclonal antiserum to pentachlorothiophenol-acetic acid-KLH immunogen: binding properties and use with heterologous PCP derivatives in ELISA for pentachlorophenol, *Anal. Bioanal. Chem.*, 2004, **379**(3), 411–418.
44 L. Guo and H. K. Lee, Electro membrane extraction followed by low-density solvent based ultrasound-assisted emulsification microextraction combined with derivatization for determining chlorophenols and analysis by gas chromatography–mass spectrometry, *J. Chromatogr. A*, 2012, **1243**, 14–22.
45 Y. Y. Chao, Y. M. Tu, Z. X. Jian, H. W. Wang and Y. L. Huang, Direct determination of chlorophenols in water samples through ultrasound-assisted hollow fiber liquid–liquid–liquid microextraction on-line coupled with high-performance liquid chromatography, *J. Chromatogr. A*, 2013, **1271**(1), 41–49.
46 E. Morita and E. Nakamura, Solid-phase extraction of antipyrine dye for spectrophotometric determination of phenolic compounds in water, *Anal. Sci.*, 2011, **27**(5), 489.
47 E. A. Zeid, A. M. Nassar, M. A. Hussein, M. M. Alam, A. M. Asiri, H. H. Hegazy and M. M. Rahman, Mixed oxides CuO-NiO fabricated for selective detection of 2-aminophenol by electrochemical approach, *J. Mater. Res. Technol.*, 2019, DOI: 10.1016/j.jmrt.2019.11.071.
48 R. H. Rakib, M. A. Hasnat, M. N. Uddin, M. M. Alam, A. M. Asiri, M. M. Rahman and I. A. Siddiquey, Fabrication of a 3,4-Diaminotoluene Sensor Based on a TiO_2-Al_2O_3 Nanocomposite Synthesized by a Fast and Facile Microwave Irradiation Method, *ChemistrySelect*, 2019, **4**(43), 12592–12600.
49 D. F. Katowah, M. A. Hussein, M. M. Rahman, Q. A. Alsulami, M. M. Alam and A. M. Asiri, Fabrication of hybrid PVA-PVC/$SnZnO_x$/SWCNTs nanocomposites as Sn2+ ionic probe for environmental safety, *Polym.-Plast. Technol. Mater.*, 2019, 1–16.
50 M. A. Subhan, P. C. Saha, M. M. Rahman, M. A. R. Akand, A. M. Asiri and M. Al-Mamun, Enhanced photocatalytic activity and chemical sensor development based on ternary $B_2O_3 \cdot Zn_6Al_2O9 \cdot ZnO$ nanomaterials for environmental safety, *New J. Chem.*, 2017, **41**(15), 7220–7231.
51 M. M. Rahman, M. M. Alam and K. A. Alamry, Sensitive and selective m-tolyl hydrazine chemical sensor development based on CdO nanomaterial decorated multi-walled carbon nanotubes, *J. Ind. Eng. Chem.*, 2019, **77**, 309–316.
52 M. M. Rahman, M. M. Alam and A. M. Asiri, Development of an efficient phenolic sensor based on facile Ag_2O/Sb_2O_3 nanoparticles for environmental safety, *Nanoscale Adv.*, 2019, **1**(2), 696–705.

53 P. Ncube, R. W. Krause and B. B. Mamba, Fluorescent sensing of chlorophenols in water using an azo dye modified β-cyclodextrin polymer, *Sensors*, 2011, **11**(5), 4598–4608.

54 M. A. Subhan, S. S. Jhuma, P. C. Saha, M. M. Alam, A. M. Asiri, M. Al-Mamun and M. M. Rahman, Efficient selective 4-aminophenol sensing and antibacterial activity of ternary $Ag_2O_3 \cdot SnO_2 \cdot Cr_2O_3$ nanoparticles, *New J. Chem.*, 2019, **43**(26), 10352–10365.

55 T. Athar, Synthesis and characterization of strontium oxide nanoparticles via wet process, *Mater. Focus*, 2013, **2**(6), 450–453.

56 Z. Mirghiasi, F. Bakhtiari, E. Darezereshki and E. Esmaeilzadeh, Preparation and characterization of CaO nanoparticles from $Ca(OH)_2$ by direct thermal decomposition method, *J. Ind. Eng. Chem.*, 2014, **20**(1), 113–117.

57 P. Pasierb, S. Komornicki, M. Rokita and M. Rękas, Structural properties of Li_2CO_3–$BaCO_3$ system derived from IR and Raman spectroscopy, *J. Mol. Struct.*, 2001, **596**(1–3), 151–156.

58 J. Nishio, M. Tokumura, H. T. Znad and Y. Kawase, Photocatalytic decolorization of azo-dye with zinc oxide powder in an external UV light irradiation slurry photoreactor, *J. Hazard. Mater.*, 2006, **138**(1), 106–115.

59 N. Morales-Flores, U. Pal and E. S. Mora, Photocatalytic behavior of ZnO and Pt-incorporated ZnO nanoparticles in phenol degradation, *Appl. Catal., A*, 2011, **394**(1–2), 269–275.

60 S. Kalathil, M. M. Khan, S. A. Ansari, J. Lee and M. H. Cho, Band gap narrowing of titanium dioxide (TiO_2) nanocrystals by electrochemically active biofilms and their visible light activity, *Nanoscale*, 2013, **5**(14), 6323–6326.

61 M. M. Khan, S. A. Ansari, D. Pradhan, D. H. Han, J. Lee and M. H. Cho, Defect-induced band gap narrowed CeO_2 nanostructures for visible light activities, *Ind. Eng. Chem. Res.*, 2014, **53**(23), 9754–9763.

62 S. A. Ansari, M. M. Khan, S. Kalathil, A. Nisar, J. Lee and M. H. Cho, Oxygen vacancy induced band gap narrowing of ZnO nanostructures by an electrochemically active biofilm, *Nanoscale*, 2013, **5**(19), 9238–9246.

63 M. M. Khan, S. A. Ansari, D. Pradhan, D. H. Han, J. Lee and M. H. Cho, Defect-induced band gap narrowed CeO_2 nanostructures for visible light activities, *Ind. Eng. Chem. Res.*, 2014, **53**(23), 9754–9763.

64 S. A. Ansari, M. M. Khan, M. O. Ansari, S. Kalathil, J. Lee and M. H. Cho, Band gap engineering of CeO_2 nanostructure using an electrochemically active biofilm for visible light applications, *RSC Adv.*, 2014, **4**(32), 16782–16791.

65 A. F. Lee, C. J. Baddeley, C. Hardacre, R. M. Ormerod, R. M. Lambert, G. Schmid and H. West, Structural and catalytic properties of novel Au/Pd bimetallic colloid particles: EXAFS, XRD, and acetylene coupling, *J. Phys. Chem.*, 1995, **99**(16), 6096–6102.

66 L. Zhang, Y. Jiang, Y. Ding, M. Povey and D. York, Investigation into the antibacterial behaviour of suspensions of ZnO nanoparticles (ZnO nanofluids), *J. Nanopart. Res.*, 2007, **9**(3), 479–489.

67 N. Talebian, S. M. Amininezhad and M. Doudi, Controllable synthesis of ZnO nanoparticles and their morphology-dependent antibacterial and optical properties, *J. Photochem. Photobiol., B*, 2013, **120**, 66–73.

68 M. M. Rahman, M. M. Alam, A. M. Asiri and M. A. Islam, Ethanol sensor development based on ternary-doped metal oxides ($CdO/ZnO/Yb_2O_3$) nanosheets for environmental safety, *RSC Adv.*, 2017, **7**(37), 22627–22639.

69 M. M. Rahman, M. M. Alam, A. M. Asiri and M. R. Awual, Fabrication of 4-aminophenol sensor based on hydrothermally prepared ZnO/Yb_2O_3 nanosheets, *New J. Chem.*, 2017, **41**(17), 9159–9169.

70 M. M. Rahman, M. M. Alam and A. M. Asiri, Fabrication of an acetone sensor based on facile ternary $MnO_2/Gd_2O_3/SnO_2$ nanosheets for environmental safety, *New J. Chem.*, 2017, **41**(18), 9938–9946.

71 M. M. Rahman, M. M. Alam, A. M. Asiri and M. A. Islam, Fabrication of selective chemical sensor with ternary $ZnO/SnO_2/Yb_2O_3$ nanoparticles, *Talanta*, 2017, **170**, 215–223.

72 M. M. Rahman, M. M. Alam and A. M. Asiri, 2-Nitrophenol sensor-based wet-chemically prepared binary doped Co_3O_4/Al_2O_3 nanosheets by an electrochemical approach, *RSC Adv.*, 2018, **8**(2), 960–970.

73 T. Wu, G. Zhao, Y. Lei and P. Li, Distinctive tin dioxide anode fabricated by pulse electrodeposition: high oxygen evolution potential and efficient electrochemical degradation of fluorobenzene, *J. Phys. Chem. C*, 2011, **115**(10), 3888–3898.

74 X. Duan, X. Sui, W. Wang, W. Bai and L. Chang, Fabrication of PbO_2/SnO_2 composite anode for electrochemical degradation of 3-chlorophenol in aqueous solution, *Appl. Surf. Sci.*, 2019, **494**, 211–222.

75 M. M. Rahman, M. M. Alam, A. M. Asiri and M. A. Islam, 3,4-Diaminotoluene sensor development based on hydrothermally prepared $MnCo_xO_y$ nanoparticles, *Talanta*, 2018, **176**, 17–25.

76 M. M. Rahman, M. M. Alam, M. M. Hussain, A. M. Asiri and M. E. M. Zayed, Hydrothermally prepared Ag_2O/CuO nanomaterial for an efficient chemical sensor development for environmental remediation, *Environ. Nanotechnol. Monit. Manag.*, 2018, **10**, 1–9.

77 M. M. Rahman, M. M. Alam and A. M. Asiri, Carbon black co-adsorbed ZnO nanocomposites for selective benzaldehyde sensor development by electrochemical approach for environmental safety, *J. Ind. Eng. Chem.*, 2018, **65**, 300–308.

78 M. M. Rahman, M. M. Alam and A. M. Asiri, Selective hydrazine sensor fabrication with facile low-dimensional Fe_2O_3/CeO_2 nanocubes, *New J. Chem.*, 2018, **42**(12), 10263–10270.

79 M. R. Karim, M. M. Alam, M. O. Aijaz, A. M. Asiri, M. A. Dar and M. M. Rahman, Fabrication of 1,4-dioxane sensor based on microwave assisted PAni-SiO_2 nanocomposites, *Talanta*, 2019, **193**, 64–69.

80 B. M. Abu-Zied, M. M. Alam, A. M. Asiri, W. Schwieger and M. M. Rahman, Fabrication of 1,2-dichlorobenzene sensor based on mesoporous MCM-41 material, *Colloids Surf., A*, 2019, **562**, 161–169.

81 M. M. Rahman, A. Wahid, M. M. Alam and A. M. Asiri, Efficient 4-nitrophenol sensor development based on facile $Ag@Nd_2O_3$ nanoparticles, *Mater. Today Commun.*, 2018, **16**, 307–313.

82 M. A. Subhan, P. C. Saha, M. M. Rahman, J. Ahmed, A. M. Asiri and M. Al-Mamun, Fabrication of a 2, 4-dinitrophenol sensor based on $Fe_3O_4@Ag@Ni$ nanomaterials and studies on their antibacterial properties, *New J. Chem.*, 2018, **42**(2), 872–881.